



IR Spectroscopy and Spectromicroscopy with Synchrotron Radiation

Paul Dumas, Michael C. Martin, and G. Laurence Carr

Contents

Introduction	2
Source Types and Characteristics	3
Dipole Bend Radiation (Conventional Synchrotron Radiation)	4
Edge, Transition, and Diffraction Radiation	9
Long Wavelength Cutoff	11
Electron Bunching, Time-Resolved, and Coherent Emission	13
Light Hazards, Optics, and Instrumentation	16
Light Hazards	16
Optics	17
Instrumentation	29
Applications	41
Spectroscopy Using Coherent Radiation	41
Spectroscopy Using Noncoherent Far-IR Synchrotron Radiation	42
Microscopy at Limited Diffraction Spot Size	44
Nanospectroscopy and Imaging	46
References	50

Abstract

Properties of infrared emission from synchrotron radiation, beamline specificities and optimization, and multidisciplinary applications are the main content of this chapter. Bending magnets are the essential source of infrared emission, and

P. Dumas (✉)

SOLEIL Synchrotron, L'Orme des Merisiers, Gif Sur Yvette, France

e-mail: paul.dumas@synchrotron-soleil.fr

M. C. Martin

Advanced Light Source, Lawrence Berkeley National Laboratory, Berkeley, CA, USA

G. L. Carr

NSLS II-Brookhaven National Laboratory, Upton, NY, USA

simplified formulas are provided to allow calculating flux and brilliance for a particular beamline. The requirements for large vertical and horizontal collection angles in this long wavelength regime impose appropriate optics to collect and propagate efficiently the beam to the instruments. Present prototypical optical setups exhibit aberration, which can be eliminated using appropriate optics described in this chapter. Example for a specific facility is given which may help improving existing beamlines. Spectroscopy and microscopy are the main approaches exploited, using commercially available instruments. These instruments are briefly described as well as the most relevant detectors used in infrared. Emerging techniques are shown, such as IR tomography and nano-infrared spectroscopy and imaging. For the latter, few beamlines operate presently a nano-infrared instrument, and several are under development. Numerous applications have been reported over the last 20 years, and for each of them, this chapter gives some examples and the related references. The recent application in nano-spectroscopy and imaging are emphasized in the application section.

Keywords

Synchrotron · Infrared · Spectroscopy · Microspectroscopy ·
Nanospectroscopy · Imaging · Bending magnet emission · Infrared beamline

Introduction

Infrared (IR) spectroscopy has become an important application of synchrotron radiation produced by an electron storage ring. In this chapter, we describe the qualities of infrared synchrotron radiation along with typical performance characteristics. We also consider the standard types of instruments used for measurements and the various techniques. Finally, some of the prototypical applications are reported.

Though there are many types of infrared sources based on electron accelerators (e.g., free electron lasers), we limit the scope to high-energy electron synchrotron/storage ring type sources. Therefore, we consider only the source types, such as dipole bending magnet radiation, that produce a continuum of photon energies (frequencies) from millimeter waves through visible light.

System of Units (S-I) are used throughout, rather than the historically more common Gaussian/CGS units. The responsivity of infrared detectors is typically in units of Volts/Watt (V/W) or Amperes/Watt (A/W), so we describe sources in terms of power rather than number of photons per second. The most commonly used unit for infrared frequencies is the wavenumber [$1/\lambda$, in units of cm^{-1}]. A useful conversion between wavenumber and photon energy is $1 \text{ meV} = 8.066 \text{ cm}^{-1}$.

We assume that the synchrotron source of interest is a storage ring employing high energy ($>500 \text{ MeV}$) electrons such that all photon energies of interest here (a few eV down to below 1 meV) are well below the critical photon energy for dipole bend sources, the latter being $100 \text{ s of eVs or higher}$. Thus, the entire infrared range corresponds to the long-wavelength limit. Similarly, we assume that the upper frequency limit for dipole edge and diffraction radiation sources is in the visible

range or higher so that the infrared properties are intrinsic to a sudden change in the electron's field during emission.

Synchrotron radiation is a unique source of infrared radiation being highly polarized, pulsed, with broad emission band, and about thousand times brighter than standard thermal source. Important applications have been and are currently achieved; among them are high-pressure studies, earth science and biology, microspectroscopy, reflectance and absorption spectroscopy for surface study, time-resolved spectroscopy, and ellipsometry. Interest in infrared synchrotron radiation goes back to the 1980s (Lagarde 1978; Stevenson and Cathcart 1980; Meyer and Lagarde 1976; Williams 1982; Duncan and Williams 1983; Stevenson et al. 1973).

Efforts to improve the radiation beam characteristics lead to elaboration of more and more sophisticated beamline optics. To achieve this goal, we need to know all characteristics of emitted radiation, its intensity distribution, polarization, and phase distribution.

Though most IR microscopy imaging makes use of the rich and unique absorption features found in the mid-IR for chemical identification, there has been increasing interest in extending the spectral range to lower frequencies, motivated in part by not only the developments in coherent THz spectroscopy and imaging but also in response to the needs of the space sciences community.

Source Types and Characteristics

This section concerns the characteristics of infrared synchrotron radiation as a source and its basic propagation. The notion that infrared from a synchrotron source can have value was initially proposed by Lagarde (1978). The most important characteristic of infrared synchrotron radiation is its very high brilliance, which is used to overcome the low throughput of many spectroscopic instruments such as for microspectroscopy. Since brilliance is typically defined in terms of photons per second per 0.1% bandwidth, we use the more practical *spectral radiance*, having units of $\text{W}/\text{m}^2/\text{rad}^2/\text{Hz}$, or the more convenient units of $\text{W}/\text{cm}^{-1}/(\text{cm}^2 \cdot \text{mrad}^2)$.

Each source type has an intrinsic polarization that can be exploited for some measurement techniques. This also affects the characteristic intensity profile at a focus. In most situations, the linearly polarized component of the source is extracted and specific polarization states are generated from that using polarization optics.

The most commonly used source of infrared synchrotron radiation is the emission from the dipole magnets that bend the electron beam around into a closed orbit. Other source types result from a sudden change in the electron's orbit or electromagnetic environment and include edge radiation, where the electron crosses the boundary between regions of different magnetic field (i.e., the edge of a dipole bend magnet). Transition and diffraction radiation, where a change in the dielectric properties along the electron's trajectory affect its Coulomb field, have not received much consideration as sources of infrared in storage rings. Transition radiation, where the electron is incident on a medium fully inserted into the beam, is not normally encountered in an electron storage ring due to the negative effect on the

electron beam itself. It shares a number of characteristics with dipole edge radiation, with the exception that the latter blends into dipole bend radiation. Diffraction radiation occurs when only a portion of the Coulomb field intercepts a different medium. This can include the changing interior dimensions found in most electron storage rings.

Undulators and wigglers – the periodic magnet structures that serve as x-ray sources – are not practical infrared sources due to the extremely long period they would require. The same issue applies to specialized structures, such as metal gratings for Smith Purcell radiation. We note that many of these other source types are very useful in lower energy electron accelerators – especially linear accelerators where the electron beam quality after the radiator is not an issue.

Dipole Bend Radiation (Conventional Synchrotron Radiation)

A standard source of infrared synchrotron radiation is from the dipole bending magnets. Details of the emission characteristics for dipole radiation were originally determined by Schwinger (1949). Two of the earliest reports on infrared synchrotron radiation came from BESSY/Berlin (Schweizer et al. 1985) and SOR/Okazaki (Nanba et al. 1986). Useful expressions for the infrared intensity and spectral dependence can be found in the work of Duncan and Williams (1983). In the long wavelength limit, the radiated intensity $P(\nu)$ (Watts) per frequency ν (in cm^{-1}) is:

$$\frac{dP(\nu)}{d\nu} = 8.64 \times 10^{-7} i \theta (\rho \nu)^{1/3} \quad (1)$$

where i is the current (amperes), θ is the horizontal angular collection (radians), and ρ is the bending radius in cm. This expression assumes integration over vertical angle, i.e., that the full angular emission is collected. Figure 1 displays the radiated intensity per frequency for three beamlines and for 100 mA of electron current.

It is interesting to compare the flux delivered by the synchrotron radiation with the spectral flux emitted by an isotropic blackbody source into a solid angle $= 2\pi \sin \theta_r$ (where θ_r is the angular radius of the first optical element of the spectrometer) (Carr et al. 2007):

$$\left(\frac{dW}{d(1/\lambda)} \right)_{BB} \left[\frac{W}{\text{cm}^{-1}} \right] \approx 3.74 \cdot 10^{-2} \frac{S_{\text{src}} [\text{mm}^2] \sin \theta_r}{\lambda^3 [\mu\text{m}]} \left[\left(\exp \left(\frac{1.44 \cdot 10^4}{\lambda [\mu\text{m}] T [K]} \right) - 1 \right) \right]^{-1} \quad (2)$$

where S_{src} is the source area.

The most important parameter is the spectral radiance comparison between a thermal source (global) and synchrotron radiation (ideal), and this is displayed on Fig. 3 in the case of NSLS II. Figure 3 also shows the effect of finite size extraction aperture and the size of the metallic vacuum chambers at NSLS II (see section “Long Wavelength Cutoff”).

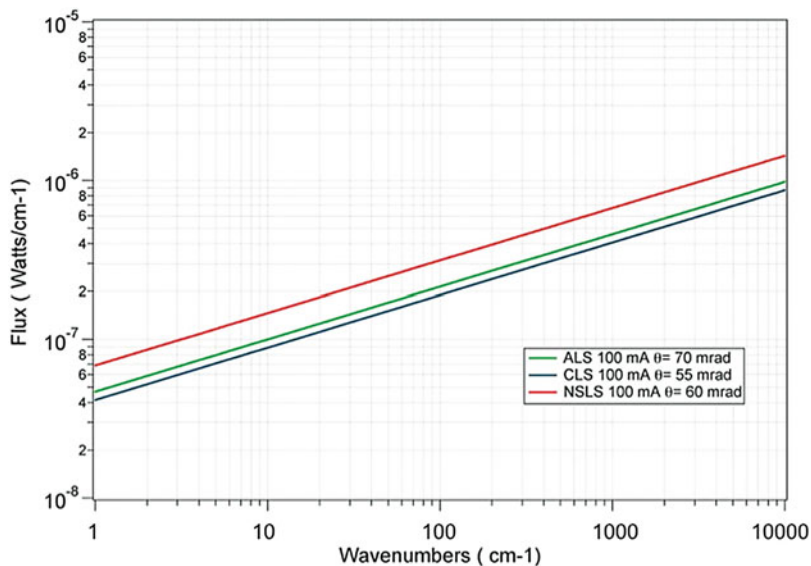


Fig. 1 Flux emitted at three beamline exploiting solely the constant field emission of a bending magnet and for 100 mA of electron current (from Eq. (1)) ($\rho_{\text{ALS}} = 4.95$ m; $\rho_{\text{NSLS}} = 25$ m; $\rho_{\text{CLS}} = 7.14$ m)

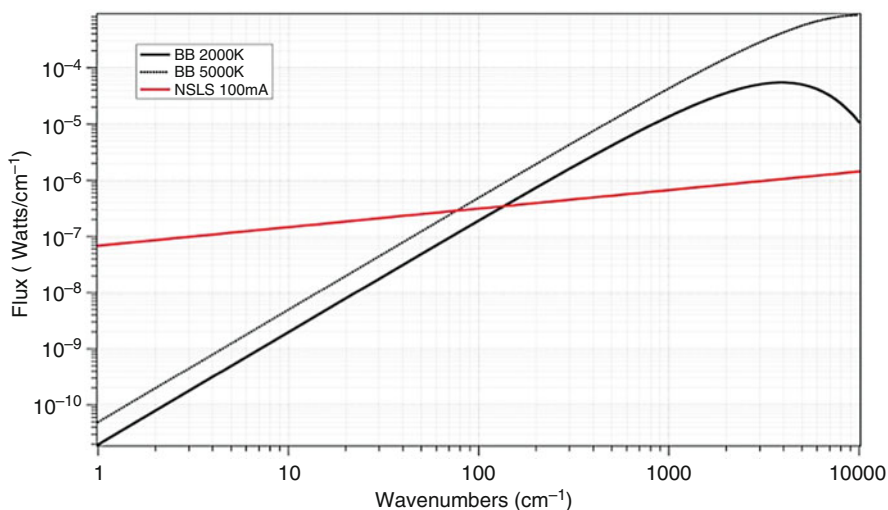


Fig. 2 Flux comparison of infrared emission from a thermal source at two operating temperatures and synchrotron radiation (at 100 mA of electron current)

The “1/3” power in Eq. (1) is ubiquitous for bending magnet radiation and stems from the source geometry. Each electron radiates continuously along an orbit of curvature ρ , with the electron falling behind its emission an amount $\rho\theta^3/6$ per

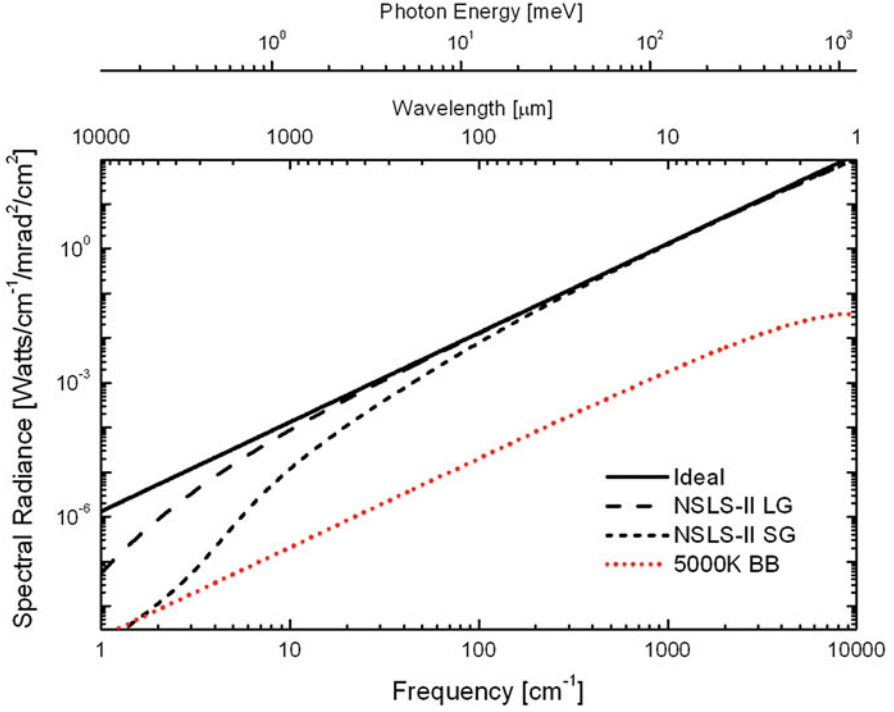


Fig. 3 Comparison of generic SR source and blackbody at $T = 5000$ K. Included with the ideal case (solid line) are calculations for two physical geometries for the NSLS-II facility (dashed lines). These include the effect of a finite-sized extraction aperture and other long wavelength cutoff effects. Note the >3 orders of magnitude advantage of the synchrotron source over the majority of the infrared spectral range

distance $\rho\theta$ along the orbit arc. The source therefore falls out of phase with the previously emitted radiation such that further emission begins to contribute to a distinctly separate radiation mode. Using the RMS value of a cosine as the cutoff point yields $\rho\theta^3/6 \approx \lambda/9$ so that $\theta_0 \approx 7/8 (\lambda/\rho)^{1/3}$. This is one derivation of the far-field angular emission for dipole synchrotron radiation in terms of the electric field strength.

The far-field intensity distribution includes both horizontally and vertically polarized components. Due to the π phase difference between the vertical components as viewed above and below the orbit plane, these interfere destructively when brought to a focus where the predominant horizontal intensity yields a maximum. As such, it does not contribute significantly for measurements where the throughput is diffraction limited. We therefore concentrate on the horizontal component alone.

The detailed vertical distribution of this light involves a rather complicated expression. Here, we provide a simple but reasonably accurate expression for this angular intensity distribution in terms of a Fermi function:

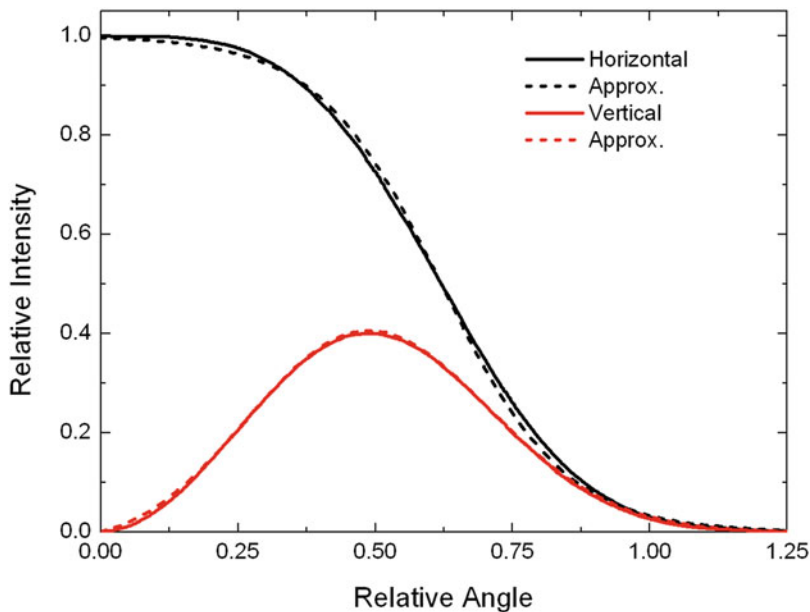


Fig. 4 Angular intensity distribution of dipole bend radiation along with results from the approximate expressions, expressed in units of $(\lambda\nu)^{1/3}$

$$I(\theta) \approx \frac{I_0}{1 + \exp \left[a \left(\theta / \theta_{\lambda\rho} - b \right) \right]} \quad (3)$$

where $a = 8.6$, $b = 0.62$, I_0 is the intensity for $\theta = 0$, and $\theta_{\lambda\rho} \equiv (\lambda/\rho)^{1/3}$. A comparison between the exact result and this approximation is shown in Fig. 4. Note that the vertically polarized component can be fairly well described by a Gaussian (offset above and below the orbit plane at $\theta = 0$).

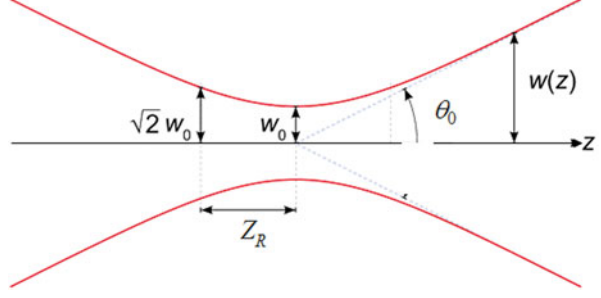
Since the intent is to focus this emission to a small illumination area on a sample, we are also interested in the Fourier transform of this function. This also provides a measure of the source's effective size. This is more readily seen in the angular distribution measured vertically, as the horizontal consists of a source continuum.

This Fourier transform of the electric field strength's angular distribution yields a function that is not much different from a Gaussian, so we provide approximate Gaussian beam parameters that can be used for estimating beam propagation through an optical system (Fig. 5).

Values for these parameters that provide a good approximation for dipole bend radiation are:

$$w_0 \approx \frac{2}{5} (\lambda^2 \rho)^{1/3} \quad \theta_0 \approx \frac{4}{5} \left(\frac{\lambda}{\rho} \right)^{1/3} \quad z_R \approx \frac{1}{2} (\lambda \rho^2)^{1/3} \quad (4)$$

Fig. 5 Diagram for a Gaussian beam focus showing definitions of the waist W_0 , the far-field angle θ_0 , and the Rayleigh range Z_R . W_0 and θ_0 represent the points where the electric field E has fallen to $1/e$ of the value directly on the z axis



where W_0 is the beam waist through a focus, θ_0 is the far-field angular divergence, and Z_R is the Rayleigh range, defined in the standard way. These expressions give the electric field $1/e$ points to within 10% accuracy and obey the usual relationships for a Gaussian beam, i.e.,

$$W_0 = \frac{\lambda}{\pi \theta_0} \quad \theta_0 = \frac{\lambda}{\pi W_0} \quad Z_R = \frac{\pi W_0^2}{\lambda} \quad (5)$$

Considering that a beam has a quality factor M^2 (for an ideal beam, the quality factor is $M^2 = 1$), one has to replace λ with $M^2 \lambda$ in each of Eq. 4. Since the far-field angular distribution only approximates a Gaussian, the M^2 value will be somewhat greater than unity, yielding a modestly larger beam waist at a focus.

Other definitions for the angular distribution are for the RMS intensity, e.g., $\theta_{\text{RMS}} = (3/4\pi) (\lambda/\rho)^{1/3}$ (Hofmann 1978), or the full angle needed for collecting 95% of the emission, e.g., $\theta_{\text{full}} = 1.6(\lambda/\rho)^{1/3}$ (Duncan and Williams 1983), which also agrees with the beam's full width $= 2W_0$ as defined by the $1/e^2$ points for the intensity. This last definition is useful for determining the dimensions of an opto-mechanical system for efficiently extracting the light.

Since each diffraction-limited source segment radiates into a full angle $\theta \sim 1.6(\lambda/\rho)^{1/3} = 1.6(\lambda\nu)^{1/3}$, we can now calculate the spectral power per such a segment as:

$$\frac{dP(\nu)}{d\nu} = 1.38 \times 10^{-6} i \text{ W/cm}^{-1} \quad (6a)$$

In this sense, as a diffraction-limited source, the long wavelength power is spectrally flat and depends only on the electron beam current. We can further multiply by e to yield the spectral energy per electron, per diffraction-limited orbit segment:

$$\frac{dP(\nu)}{d\nu} = 2.2 \times 10^{-25} \text{ J/cm}^{-1} \quad (6b)$$

The expressions in (6a) and (6b) allow for simple performance comparisons with other source mechanisms.

Edge, Transition, and Diffraction Radiation

Edge radiation occurs where an electron crosses a boundary between two different magnetic field strengths. The most common example is where an electron enters or exits the dipole field of a bending magnet. Here, the Coulomb field of the electron moving in a straight line is replaced with the field of an electron on a curved orbit. This abrupt change results in radiation that propagates in the forward direction, i.e., parallel to the electron's velocity as it crosses the field's edge. Transition and diffraction radiation are types of sources in which some, or all, of the electron's Coulomb field is modified due to the presence of a medium having a different electromagnetic response. Transition radiation refers to the situation where the entire Coulomb field is affected (e.g., due to being incident onto an object such as a metallic mirror), whereas diffraction radiation occurs when a portion is affected (e.g., passing near to an object). These two types of sources are usually considered only for accelerators other than storage rings, due to the major disruption of the electron's trajectory resulting in beam loss. However, they can be useful sources for diagnosing beams in linear accelerators and injection systems.

For transition radiation from an electron crossing from vacuum to a good conductor, the entire Coulomb field of a charge moving at a constant velocity is abruptly removed. The opposite occurs for an electron emerging from a conductor into vacuum. This time-dependent Coulomb field exhibits the same behavior as for edge radiation where an electron enters or exits a dipole field, and the expressions for the emitted radiation are the same. However, since edge radiation sources are directly connected to dipole bends, the far-field emission is a superposition of the two, and aspects of their emission can be difficult to distinguish experimentally. This can be seen in results from computer codes for calculating synchrotron radiation, such as SRW (Chubar et al. 2002, 2007).

To understand edge (and transition) radiation, we begin with the Coulomb field of a relativistic electron moving at a constant velocity, which is highly compressed in the direction transverse to the electron's velocity. The cross section of this field (Jackson 2007) increases with distance from the electron, having a half-width at half maximum of $2b/\gamma$, where b is the distance from the electron (i.e., the impact factor). The $1/e$ distance for radiating at wavelength λ is $W_0 = \lambda\gamma/4\pi$. We note that the transverse electric field and intensity for edge and transition radiation fall-off much more slowly with distance than a Gaussian, so the usual relationships between Gaussian beam parameters are not accurate. Additionally, the orientation of the Coulomb field results in a radially polarization emission similar to the L_{01} "doughnut" mode, which is the superposition of two orthogonally polarized L_{01} modes, each having a quality factor of $M^2 = 3$ (Herman et al. 1998). In practice, the $1/e$ point of the electric field ($1/e^2$ for the intensity) relative to the maximum at

$\theta = 1/\gamma$ defines a far-field half-angle $\theta_0 \approx 5/\gamma$. The RMS value is about three times larger, suggesting an M^2 closer to 3.7.

The far-field angular distribution of radiated spectral energy per electron is given by:

$$\frac{dE(\theta, \omega)}{d\omega} = \frac{e^2}{4\pi^3 \epsilon_0 c} \frac{\beta^2 \sin^2 \theta}{(1 - \beta^2 \cos^2 \theta)^2} \quad (7)$$

Note that, once again, the source is spectrally “flat.” Integrating overall angles yields the total spectral energy:

$$\frac{dE(\omega)}{d\omega} = \frac{e^2}{4\pi^2 \epsilon_0 c} \left[\ln \left(\frac{2}{1 - \beta} \right) - 1 \right] \text{ J/rad/s} \quad (8a)$$

or in wavenumber units:

$$\frac{dE(\nu)}{d\nu} = 4.62 \times 10^{-26} \left[\ln \left(\frac{2}{1 - \beta} \right) - 1 \right] \text{ J/cm}^{-1} \quad (8b)$$

Assuming a 1 GeV electron, the factor in square brackets is about 15.5 such that the energy per wavenumber becomes $7.1 \times 10^{-25} \text{ J/cm}^{-1}$. Note that this is just over a factor of 3 greater than for the dipole bend source (cf. Eq. 6b). However, there is not a significant benefit in brilliance due to the larger M^2 of transition radiation (and edge radiation). Therefore, the choice of source type for developing an infrared source is more dependent on other considerations such as mechanical constraints of the accelerator system itself. For a beam of current i , the power is:

$$\frac{dP(\nu)}{d\nu} = 2.88 \times 10^{-7} i \left[\ln \left(\frac{2}{1 - \beta} \right) - 1 \right] = 4.47 \times 10^{-6} i \text{ W/cm}^{-1} \quad (8c)$$

Thus, the integrated intensity for a beam current of 0.5A at 1 GeV and the spectral range extending up through the visible ($25,000 \text{ cm}^{-1}$) is about 55 mW. Figure 6 shows a sketch of two edges sources which are typically collected for infrared radiation. One challenge for extracting edge radiation is the fact that dipole edges usually come in pairs, i.e., when viewing the emission from an electron entering a given dipole, the emission occurring from where the electron exits the previous (upstream) dipole strongly overlaps and interferes. The intrinsic phase difference for the two sources is π , resulting in destructive interference directly on-axis. Path differences for an off-axis observer result in a series of ring-like intensity fringes.

The degree to which the fields overlap and interfere depends on details of the electron beam vacuum chamber in the region between the two dipoles.

Details for diffraction radiation depend heavily on the shape and location of the radiating interface relative to the electron beam. The short wavelength limit for the emission is expected to obey:

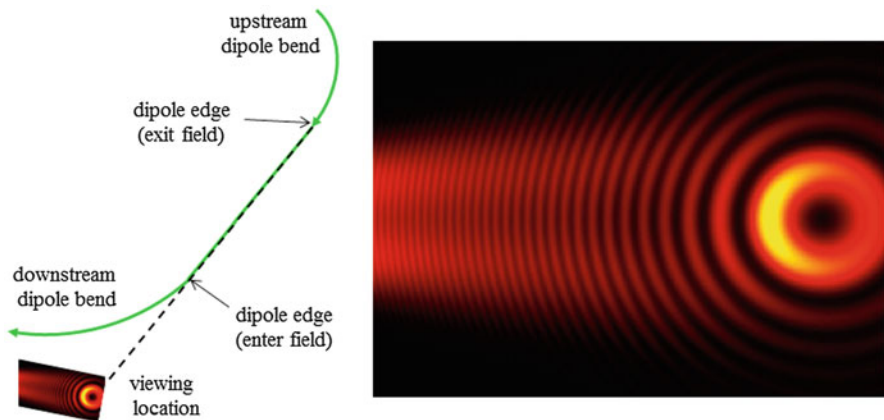


Fig. 6 Infrared intensity through an aperture located downstream of two sequential dipole bend magnets. The continuum of light extending to the left is the dipole bend radiation from the nearest (downstream) dipole. The ring-shaped intensity fringes are due to interference between the two edge sources. Calculation using SRW code

$$\lambda_{\text{diff}} \geq \frac{4\pi b}{\gamma} \quad (9)$$

where b is the minimum distance between the edge of the radiator and the electron beam. For a typical 3 GeV electron beam and a minimum distance of 2 cm, the emission is limited to wavelengths longer than about 40 μm (250 cm^{-1}), i.e., in this would be a strictly far-infrared source.

Long Wavelength Cutoff

With few exceptions, an electron accelerator serving as a light source has the electron beam contained in a metallic vacuum chamber. The boundary conditions this imposes on the electron's Coulomb field results in a long wavelength limit for producing radiation. This can be visualized as the superposition of multiple sources (the actual electron plus its image charges) radiating and overlapping with opposite phases. Figure 7 shows a schematic representation of the vacuum chamber acting as a waveguide cutoff.

For dipole bend radiation, a strong cutoff exists for wavelengths longer than:

$$\lambda_C \cong \sqrt{\frac{2h^3}{\rho}} \quad (10)$$

Note that this value corresponds to when the effective source width W_0 is $\frac{1}{2}$ of the chamber height. Typical values for h are $\sim 2\text{ cm}$ and $\rho \sim 10\text{ m}$, such that

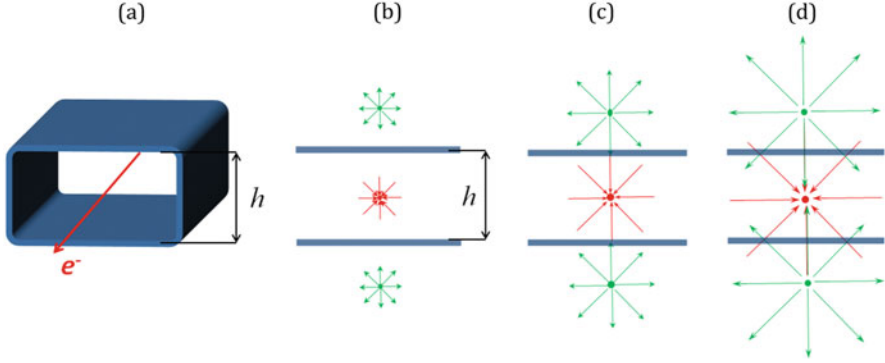


Fig. 7 Schematic illustration of the waveguide cutoff. An example chamber cross section is shown in (a) where the height is smaller than the width. Panels (b) through (c) show the radiating portion of the Coulomb field for increasing wavelength. For simplicity, only the top and bottom walls are considered. The electron's field, ignoring the boundary conditions, is shown in red, while the additional fields for the first set of image charges are shown in green. Note that the source fields begin to overlap in (d), leading to a net reduction of the horizontal field components. The vertical fields are enhanced at first, but those eventually cancel as well with increasing wavelength

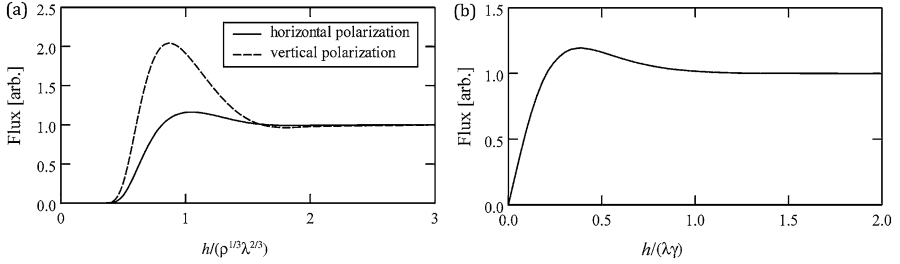


Fig. 8 Calculated flux between two infinite conducting sheets placed a distance $h/2$ above and below the electron beam for (a) dipole bend radiation and (b) edge radiation. Note the predicted flux enhancement as the wavelength nears the cutoff value, especially for the vertically polarized dipole bend source. (From Bosch 2002)

$\lambda_C \sim 0.125 \text{ cm}$ (8 cm^{-1}) for the dipole bend sources. In the case of NSLS-II large gap dipoles ($h = 7.6 \text{ cm}$ and $\rho \sim 25 \text{ m}$), the cutoff is at $\lambda_C = 0.6 \text{ cm}$ (1.7 cm^{-1}).

We can also consider edge radiation in a similar manner. Setting $\lambda_C \gamma / 4\pi = h/2$ to define a cutoff wavelength due to shielding from a metal vacuum beam pipe yields:

$$\lambda_C \cong \frac{2\pi h}{\gamma} \quad (11)$$

which corresponds well to the point where the emitted intensity should be falling most rapidly as a function of increasing wavelength (Bosch 2002). To date, little experimental data exists to confirm the calculations for the edge source (Fig. 8).

Assuming 3 GeV electrons inside a metal beam pipe having 2.5 cm interior dimension, the emission is significantly reduced for wavelengths greater than $\sim 27 \mu\text{m}$ or for frequencies below $\sim 375 \text{ cm}^{-1}$. This suggests edge radiation is not a useful source for reaching into the far infrared. Additionally, for all types of sources, the far-field emission tends to fill greater angles as the wavelength increases toward the cutoff, further challenging the ability to collect it efficiently.

Electron Bunching, Time-Resolved, and Coherent Emission

The radiated energy of the electrons is restored by the electric field in a radio frequency (RF) cavity, resulting in bunching of the orbiting electrons. The radiation is therefore pulsed, with duration ranges from picoseconds to nanoseconds, depending on the RF frequency and voltage as well as the energy spread of the electrons in combination with the storage ring's dispersion. This is not unique to the infrared but applies to the entire radiated spectrum and can be exploited for a number of time-resolved methods. In a typical storage ring ($\sim 500 \text{ MHz}$ RF and 250 mA average current), each bunch contains about 3×10^9 electrons, randomly distributed with an approximately Gaussian longitudinal density distribution. Their relative distance, scaled by the wavelength of interest, determines the phase difference for their emission. For wavelengths smaller than the bunch length, the random positions lead emission having random phases. The result is a longitudinally incoherent waveform where the intensity that scales linearly with the number of electrons, i.e., the instantaneous beam current.

In general, the on-axis spectral intensity $dI/d\omega$ for multiple particles where the phase differences are only due to the longitudinal distribution is (Nodvick and Saxon 1954):

$$\frac{dI(N)}{d\omega} = [N + N(N - 1) f(\omega)] \frac{dI(1)}{d\omega} \quad (12)$$

where N is the total number of particles and $dI(1)/d\omega$ is the spectral intensity for a single particle. The function $f(\omega)$ is a longitudinal form factor defined as:

$$f(\omega) = \left| \int_{-\infty}^{\infty} e^{i\omega z/c} S(z) dz \right|^2 \quad (13)$$

where $S(z)$ is the longitudinal particle density along the direction of propagation z , assumed the same as the electron's velocity.

Since most storage rings have RMS bunch lengths greater than 10 ps (under normal operating conditions), the spectral range for coherent emission is below about 30 GHz (a wavelength of about 1 cm), which is beyond the cutoff limit determined by the electron beam's metal vacuum chamber (see section “[Long Wavelength Cutoff](#)”) so is typically not observed. Also, note that this is distinct from transverse coherence as determined by the lateral dimensions of the electron beam

and angular range of emission. In other words, the emission can have transverse coherence but lack longitudinal coherence.

Under special operating conditions, shorter bunches with a non-Gaussian longitudinal distribution can develop and coherent radiation shorter than the chamber cutoff can be produced (Abo-Bakr et al. 2002; Carr et al. 2001). This also improves the time resolution for all emitted wavelengths. The strong interaction between the electrons themselves can result in instabilities that limit the electron density in a bunch and the overall current that the storage ring can support. For this reason, the operation of a storage ring source in this special “mode” is usually limited to a few weeks each year. Other operating modes, such as with special fill patterns of the electrons around the ring to achieve specific pulse repetition frequencies, are not specific to infrared so are not addressed here.

Successful uses of coherent synchrotron radiation in storage rings started when the storage ring operated with small momentum compaction factor, which is a method to reduce the bunch length and reach the coherent emission boundary (Barros et al. 2013).

The momentum compaction or momentum compaction factor is a measure for the momentum dependence of the recirculation path length for electrons bound in cyclic motion (closed orbit).

CSR occurs in electron storage rings when the wavefronts emitted by electrons within a bunch superimpose at equal phase. The resulting source power has a quadratic dependence to the number of electrons per bunch.

Machine physicists are able, at specific storage rings, to manipulate the electron bunch length and shape by tuning the storage ring optics, the so-called “low alpha” mode (Wiedemann 1993), where alpha, α , is the momentum compaction factor describing the orbit length variation with beam energy.

According to Abo-Bakr et al. (2003), for a given radiation wavelength, λ , the emitted power, P , can be derived from the “incoherent,” single particle power, $P_{1, \text{incoherent}}$:

$$P = N \cdot P_{1, \text{incoherent}} (1 + N f_\lambda) \quad (14)$$

where f_λ is a form factor, derived from the Fourier transform of the longitudinal electron density in the bunch.

For $f_\lambda \gg 1$, phase correlation is achieved and mostly coherent synchrotron radiation (CSR) is emitted.

If the bunch density distribution is Gaussian, with RMS length σ , the form factor is given by:

$$f_\lambda = \exp \left[-(2\pi\sigma/\lambda)^2 \right] \quad (15)$$

Reducing the bunch length (σ) favors CSR emission at long wavelengths.

α can be changed at a fixed voltage delivered by the RF cavities, and the “zero current” bunch length can be varied as $\sigma = \sigma_0 \cdot f_s/f_{s0}$, where the “0” subscript

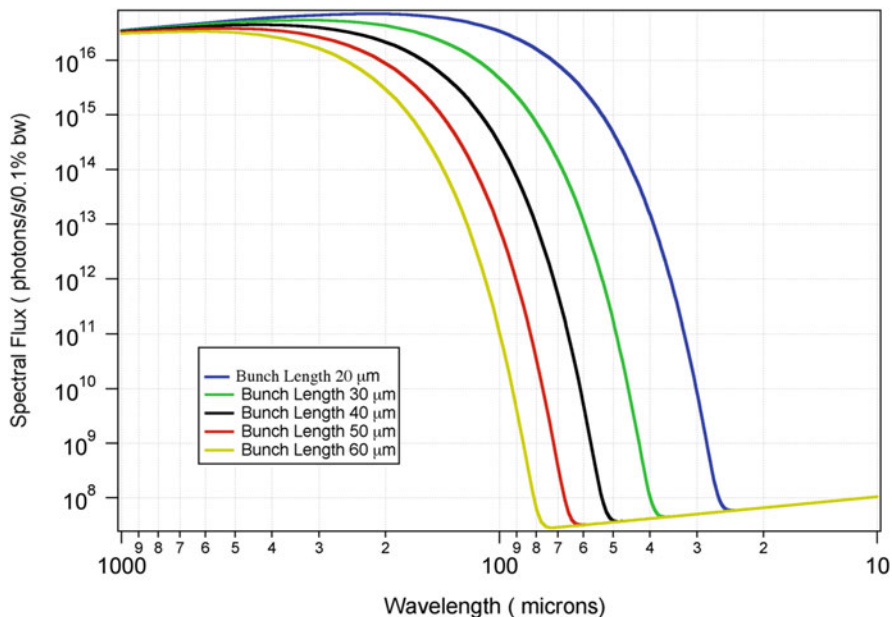


Fig. 9 Bunch length dependency of the spectral range of CSR. Calculations performed using SRW with the following parameters: $E = 3$ GeV; $I = 0.01$ Amp; $B = 1.4$ T; horizontal mixed moment = -0.89 nm \cdot rad; vertical mixed moment = -332 nm \cdot rad

refers to the operating parameters of the regular user operation. With the low alpha optics, f_s could be reduced by more than a factor of 10, corresponding to a 100 times smaller α .

The spectral range depends on the longitudinal shape of the electron bunch but can be widened towards high frequencies by reducing the bunch length (Fig. 9).

Decreasing the bunch length favors a more extended spectral range for coherent emission and may allow increasing tremendously the flux towards the mid infrared region. The THz range in particular is reached with a bunch length equivalent to a few picoseconds emission. The emitted flux is several orders of magnitude compared to noncoherent emission, even at high current intensity (Fig. 10).

The bunch length in a storage ring varies with the current, but in a first approximation, it depends on the energy of the electrons, on the radiofrequency cavity voltage, and on the momentum compaction factor α .

Coherent emission at wavelengths shorter than the chamber cutoff was first observed at NSLS (Upton) (Carr et al. 2001) and MAX Lab (Lund). Stable coherent emission was developed at BESSY II and other SR facilities, including the Metrology Light Source (PTB, Berlin) and SOLEIL (France) (Barros et al. 2013).

Coherent emission has also been observed as a consequence “laser slicing” (Byrd 2005; Shimada et al. 2007), where the energy of electrons in a subpicosecond section of a longer electron bunch is modulated by interaction with a strong laser pulse. The

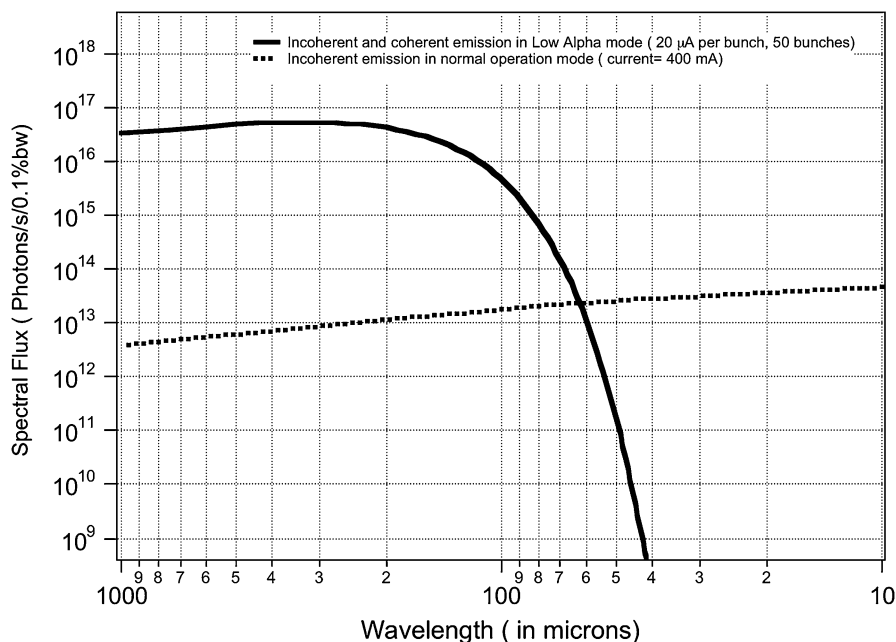


Fig. 10 Comparison of the spectral flux with a coherent emission in low alpha mode (20 μ A per bunch, 50 bunches) and incoherent emission in normal operation mode, with an electron current of 400 mA. There are several orders of magnitude more flux in the spectral range below 100 microns (~ 3 THz). Calculations performed using SRW

ring's dispersion causes these electrons to shift away from their normal location in the bunch, leaving a "hole." This density modulation results in coherent THz emission.

Light Hazards, Optics, and Instrumentation

Light Hazards

A simplifying feature of an infrared beamline over one designed to extract and deliver x-rays is that conventional mirror optics can be used for collecting and transporting the light from inside the accelerator shielding to a location where infrared instruments can be operated. The reflectance from a mirror with a simple metal coating can be very high even when used to change the beam direction by 90° . Therefore, a typical infrared beamline delivers its light around the fixed shielding of the accelerator to a location where no ionizing radiation is present. This does not necessarily eliminate all potential source hazards. The light itself can have sufficient intensity to fall into one of the laser hazard categories, requiring that the beam be controlled inside a contained environment.

Optics

First Mirror

The first optical component of an infrared beamline is, for all the existing ones so far, a flat mirror. This mirror is used to deviate the radiated photons either vertically or horizontally out of the bending magnet environment in to position a second optical element, either a flat mirror again or a first focusing mirror.

This first mirror, often called the extraction mirror, is one of the most delicate components of the beamline which needs a precise positioning and shaping for specific reasons related to the extraction of the infrared photons:

- It is often located in the dipole chamber inside the bending magnet or between the exit of the bending magnet and the first quadrupole, or after the sextupole, and may or may not be isolated from the vacuum of the storage ring by a gate valve, for any maintenance reason.
- The mirror must remain undamaged by the huge power density of the emitted synchrotron radiation that reaches this first mirror.
- During machine studies, or motion of the electron beam, it needs to be moved away from the orbit and repositioned precisely for collecting the radiated photons.

The most critical parameter to cope with when inserting such a mirror is the power density of the impinging photons emitted from the bending magnet.

The radiation power generated from a dipole magnet is uniform in the plane of the orbiting particles (or horizontal plane). In the direction transverse to this plane, the bending magnet power has a nearly Gaussian profile with its peak in the horizontal plane.

The bending magnet power distribution can also be expressed as (Khounsary and Lai 1992):

$$\frac{d^2 P}{d\theta \cdot d\psi} = \frac{1.44e^{-18}}{\rho} \cdot \gamma^5 \cdot F(\gamma\psi) \quad (16)$$

$\frac{d^2 P}{d\theta \cdot d\psi}$ is expressed in W/mrad θ .mrad ψ .mA and is the radiated power from a bending magnet of radius ρ [m] at a vertical angle ψ into a one mrad² “solid” angle with a charged particle beam current of 1 mA. As the first mirror accepts only a part of the total bending magnet radiation, the horizontal acceptance θ is restricted.

The factor $F(\gamma\psi)$ is given by:

$$F(\gamma\psi) = \left(1 + \gamma^2\psi^2\right)^{-5/2} \left[\frac{7}{16} + \frac{5}{16} \frac{\gamma^2\psi^2}{(1 + \gamma^2\psi^2)} \right] \quad (17)$$

Integrating (17) with respect to $\gamma\psi$, and noting that $\int_{-\infty}^{+\infty} F(\gamma\psi) d(\gamma\psi) = \frac{2}{3}$.

One gets, for the vertically integrated bending magnet:

$$\frac{dP}{d\theta} = 0.96 \times 10^{-15} \frac{\gamma^4}{\rho[m]} \text{ in W/mrad } \theta/\text{mA}$$

The power density peaks at $\theta = 0$, and, according to (17) is equal to:

$$\left. \frac{d^2P}{d\theta \cdot d\psi} \right]_{\psi=0} = 0.63 \times 10^{-18} \frac{\gamma^5}{\rho[m]} \text{ in W/mrad}^2 \cdot \text{mA} \quad (18)$$

SRW is used to compute the power density integrated overall photon energies for synchrotron radiation emitted by an electron beam with nonzero emittance in arbitrary magnetic field. The computation provides the power density distribution (heat load) in a transverse plane located at a certain distance from the SR emission region.

Since the natural vertical opening angle increases with decreasing energy (or increasing wavelength), the highest power density is concentrated around the orbit axis (Fig. 11), outside the infrared photon peaks.

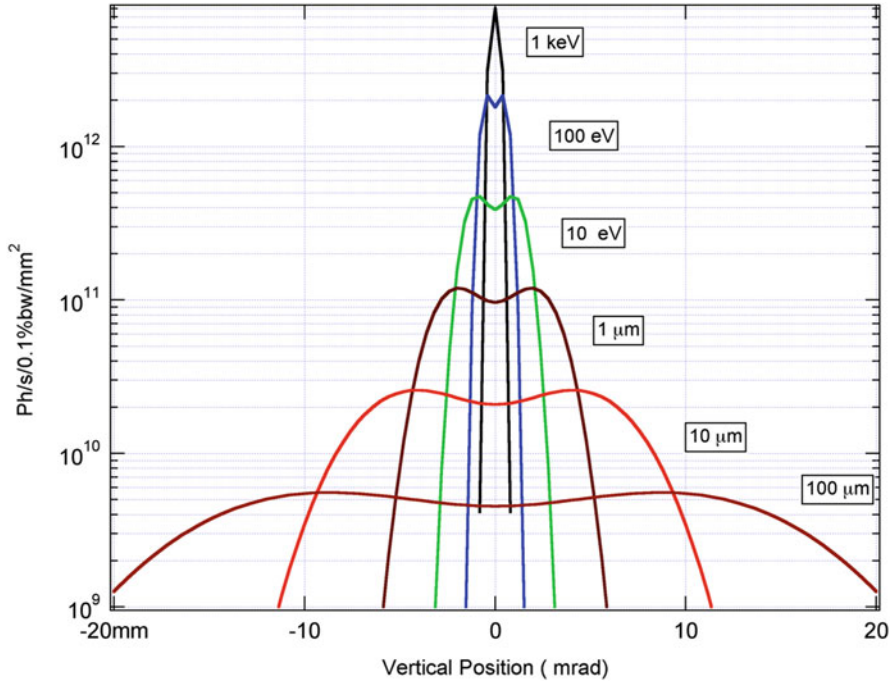


Fig. 11 Flux density as a function of energy, within an aperture of 40 mrad, and for $E = 3$ GeV, $B = 1.42$ T, and $I = 100$ mA. The highest flux are those for short wavelength and are concentrated around the horizontal axis

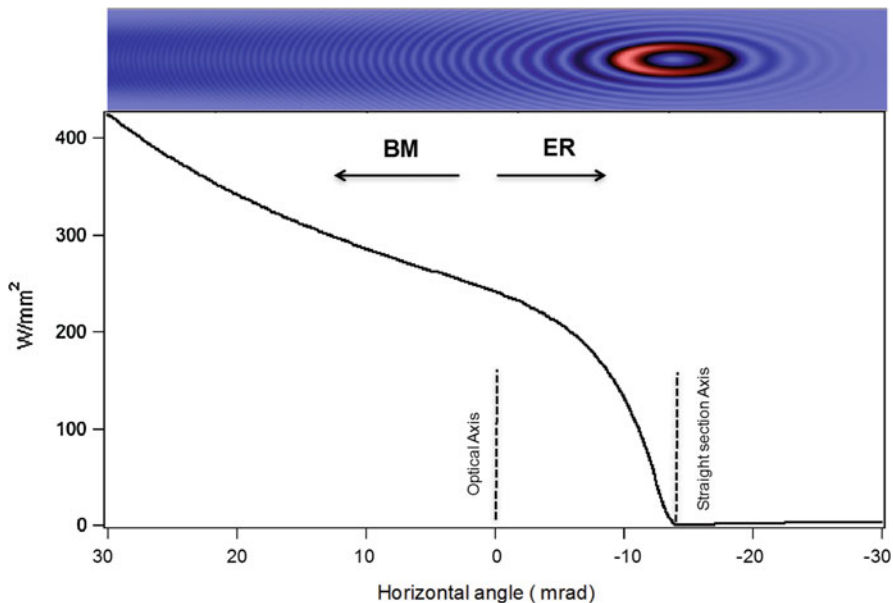


Fig. 12 Flux density along the horizontal axis, in the orbit plane, for the collection of ER and BM infrared radiation. Note that the optical axis has been moved away from the straight section axis, in order to collect the optimum number of photons from these two sources. The calculations has been carried out for $E = 3$ GeV, $B = 1.42$ T, $I = 400$ mA, and $H \times V = 60 \times 20$ mrad². The wavefront profile at 10 mm wavelength is displayed on top of the figure (vertical not in scale)

In many facilities, infrared photons have been collected using both edge radiation and constant field emission. The power density is markedly evolving along the horizontal axis, since it approaches zero along the straight section axis, and gradually increase with the motion of the charged particle inside the constant field of the bending magnet, as shown in Fig. 12.

Obviously, the power density becomes very high in the constant field emission (BM), and such a power should be screened in order to avoid any mirror damage.

The first optical component of infrared beamline exhibits either a slot or a water-cooled mask.

Protecting the first mirror by a slot of a mask is, somehow, detrimental for the photon flux that is reflected from this first optical element. In the meantime, the power density should be kept low.

The vertical distribution of the photons in the mid infrared region is larger than the power density distribution and help determining the precise size of the slot that is needed for the design of the first optical component of an infrared beamline (Fig. 13).

Determining the appropriate slot size (or mask dimension) is a tradeoff between the power density left on the mirror, the lost of flux versus wavelength, and the electron beam stability issues. This last parameter has become less than a problem

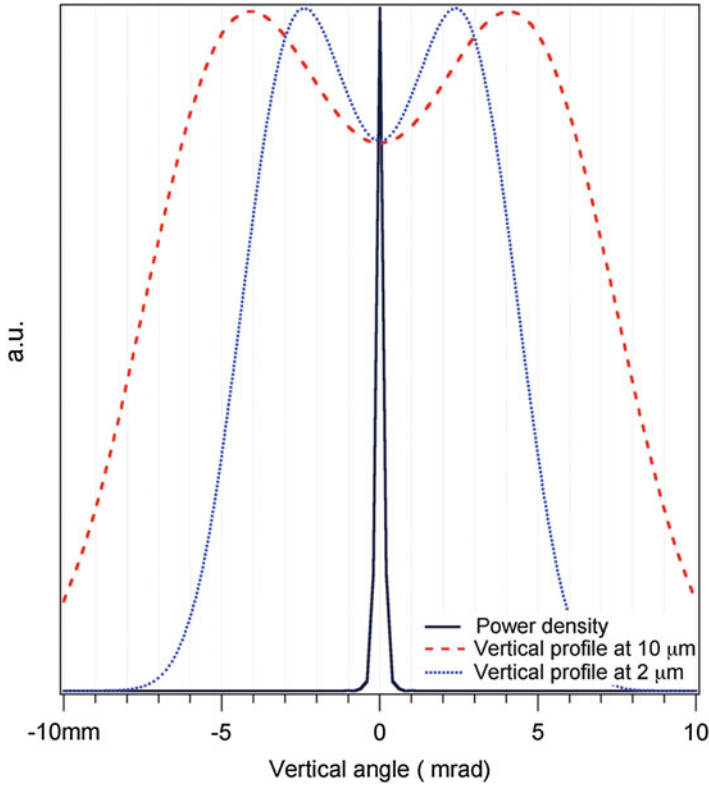


Fig. 13 Power density distribution along the vertical angle, compared with that of a $10\ \mu\text{m}$ and a $2\ \mu\text{m}$ wavelength. The simulation has been carried out with $E = 3\ \text{GeV}$, $B = 1.4\ \text{T}$, and aperture $= 20 \times 20\ \text{mrad}^2$

with the third generation synchrotron. The electron beam stability has tremendously improved, and reasons for such instabilities can be investigated (Lerch et al. 2012).

First mirror at infrared beamline are usually water cooled (even though care has to be taken on avoiding any fluid turbulences that could induces parasitic frequency which are detected on infrared spectra) or cold nitrogen flow.

Beam Propagation

The general layout for beam propagation is composed by focusing optic (elliptical or toroidal mirror) that creates an image of the source near an infrared transparent window (in most cases, a diamond window). After the first focus, a general optical setup includes two cylindrical mirrors (one tangential and one sagittal) to collimate the beam for its propagation towards the spectrometer, as well as reshaping the beam to an adequate size fitting with the entrance pupil of the spectrometer.

Figure 14 displays a conventional optical setup for the extracted IR beam.

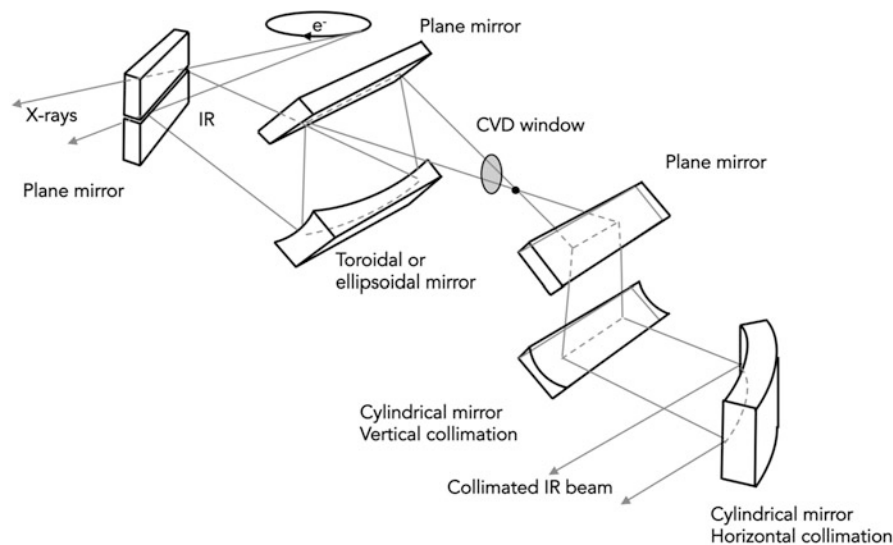


Fig. 14 Most conventional optical setup for infrared beam propagation

After the first plane mirror situated in the dipole chamber (either with slot or mask in its central horizontal section), a focusing optical element (ellipsoid or toroid) deviates the beam either downward or upward in order to extract the beam not in the orbit plane and out of the storage ring. The beam is focused on a broadband infrared transparent window (the most common one being of a thin diamond window, wedged to avoid Fabry-Perot interferences). After this window, that separates the ultrahigh vacuum of the storage ring to the purged pipe lines or vacuum of the remaining beamline, plane, and cylindrical mirrors (or elliptical/toroidal, parabolic) located after the first focus point have the purpose to move the beam, after collimation up or down for a propagation at the spectrometer entrance plane. Other geometries can be chosen. In this section, we will consider the most common one: propagation of a collimated beam.

For constant field radiation of a bending magnet, several optimization softwares are available and very appropriate for defining the characteristics of each optical element: ray tracings (Shadow, Rays, SPOTX, Xemax . . .) and wavefront propagation (SRW).

SRW is the most appropriate software for the propagation of edge radiation, since the propagation of wavefront accounts for the near-field effect, which is hardly account for with ray tracing softwares.

The following example illustrates the comparison of the ray tracing software and SRW in the propagation and focalization of $10\text{ }\mu\text{m}$ wavelength radiation, and for the following parameters: $E = 2.9\text{ GeV}$, $\rho = 7.14\text{ m}$, aperture: $55 \times 38\text{ mrad}^2$, first mirror located at 1.11 m from source, constant field radiation (BM), focusing optics = toroidal mirror, at 2.31 m from source, tangential radius = 3.54 m , sagittal

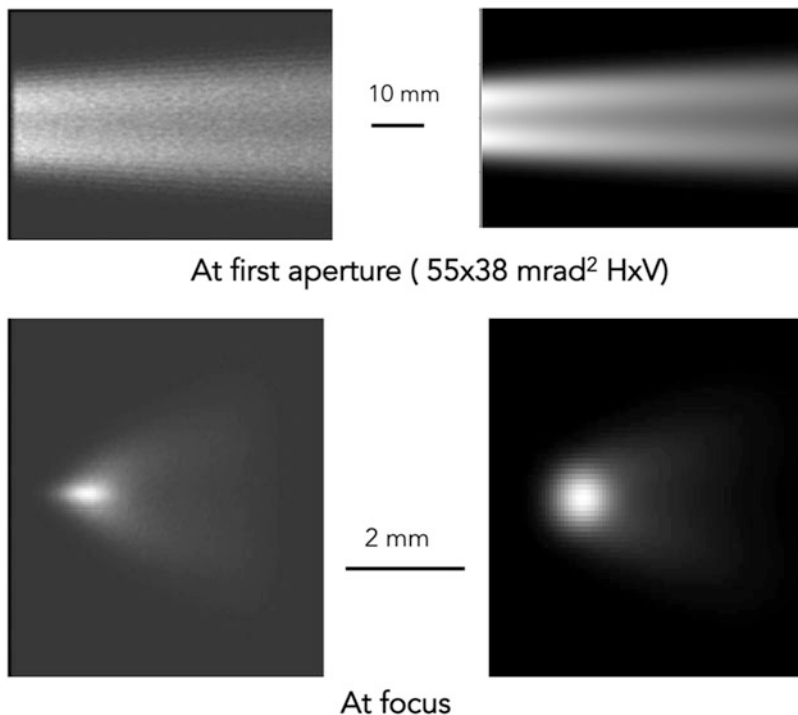


Fig. 15 Intensity profile of a $10\ \mu\text{m}$ wavelength at the first aperture and at focus. Left – simulation using SPOTX; right – simulation using SRW

radius = 1.77 m, and focal point at 2.9 m from source. The beam profiles at the first mirror and at the first focus, simulated using either a ray tracing software (SPOTX) (Moreno and Idir 2001) or SRW, are displayed on Fig. 15.

This example illustrates the excellent agreement between ray tracing and wave-front propagation approaches.

The source image produced by focalization with the toroidal mirror exhibits tails that originate from the geometrical aberrations produced by the circular shape of the bending-magnet source. These aberrations grow as the square of the horizontal beamline aperture (Fig. 16).

As a matter of fact, large horizontal collection angle makes very difficult to properly collimate the beam for an efficient propagation and coupling with the instruments: shape and collimation are hardly kept for beam propagating at several meters away from the last optical element, as it is generally the case in almost all synchrotron facilities (Fig. 17).

Aberration-Free Optical Setups

The photon source size results from the convolution of three terms: the geometrical aberrations produced by the circular shape of the electron trajectory (synchrotron

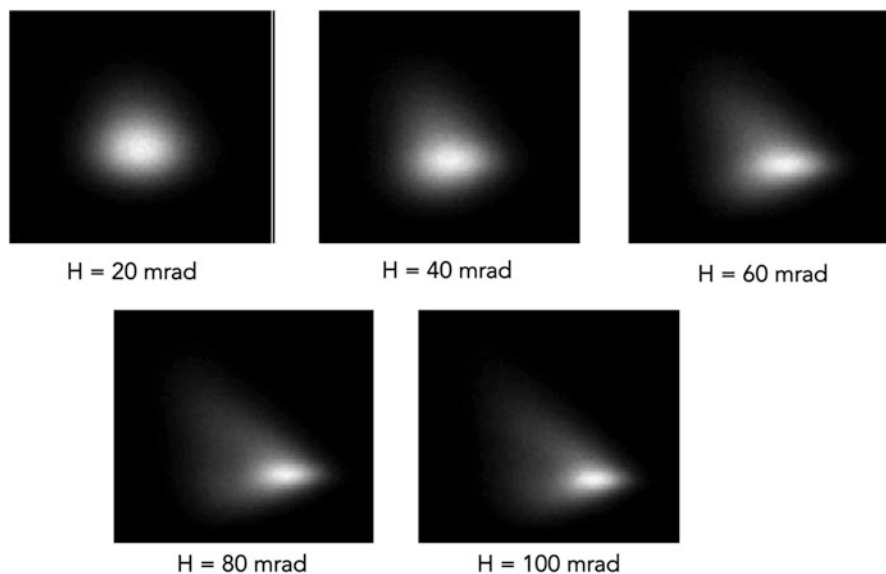


Fig. 16 Increased geometrical aberrations, observed at the secondary source (first focalization), with the horizontal angle of collection, due to the circular shape of the source. The simulation have been carried out with SPOTX, with a vertical collection angle of 30 mrad and a wavelength of 10 μm

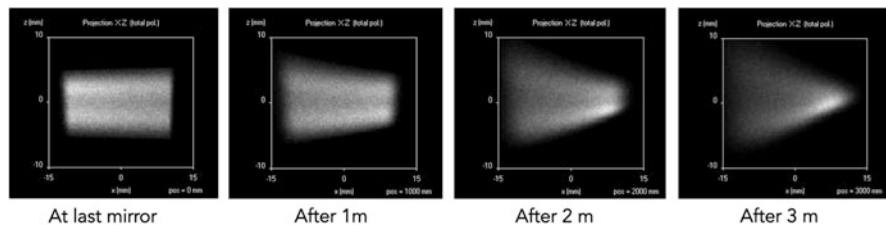


Fig. 17 Beam profile at 10 μm wavelength, along its collimated pathway from the last mirror up to 3 m away for this mirror (horizontal opening angle = 80 mrad)

radiation mode), the electron beam size, and the diffraction limit (Hecht and Zajac 1987). When the geometrical aberrations are small, for example, for restricted beamline apertures or for very large wavelengths as in the far IR, the horizontal and vertical profiles of the photon source are Gaussian, whereas for large extraction apertures, the geometrical aberrations prevail, and the profiles maintain the aberrations of the source shape. In this case, the horizontal profile of the source emission resembles the one obtained from reflection through a cylindrical mirror and retains the aberrations resulting from the circular shape of the bending magnet source. In the vertical direction, the profile is Lorentzian and is formed by the overlapping of all the vertical emissions produced at each point in the electron trajectory.

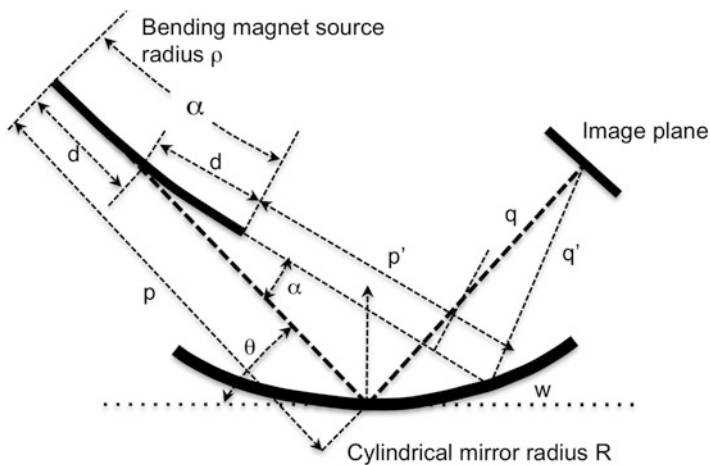


Fig. 18 Focusing the horizontal source with an aberration scheme, using a cylindrical mirror (Moreno 2015)

The first attempt to reduce the geometrical aberrations in the optical design of an infrared beamline was achieved at SPring-8 (Kimura et al. 2001). Considering the large bending magnet radius (39.3 m, $B = 0.679$ T) of the beamline with acceptance angles of 36.5×12.6 mrad² ($H \times V$) at this 8 GeV storage ring, the emission length (source depth) being 1.44 m, the formula of a perfect focusing mirror for the circular orbit, a so-called “magic mirror” proposed by López-Delgado and Szwarc (1976) has been extended to account for the vertical direction and to calculate the 3D magic mirror actually in use at (BL43IR) at SPring-8 (Kimura et al. 2001).

Such surface is very complex because of the nonspherical and no symmetric shape of such a mirror, and, in order to fabricate such complex mirror, numerical cutting methods are mandatory. The performances obtained at SPring-8 are in very good agreement with the simulations. One of the drawbacks of such mirror is the excessive cost for fabrication.

More recently, T. Moreno (2015) has provided another solution, which is explained in more details in the following. Two mirrors, a cylindrical and a cone-shaped one, focus independently the horizontal and the vertical emission, respectively. A cylindrical mirror in tangential reflection with a coma aberration source can produce a point-like aberration-free image at a fixed combination of grazing incidence and focal distance.

We detail, in the following, the formulas developed in the above article, followed by an example, that could help designing new Infrared beamline accounting for these aberration issues.

The top view of the cylindrical mirror in tangential reflection, focusing the cylindrical shape of the synchrotron source, is shown in Fig. 18.

The method followed by T. Moreno (2015) consists of minimizing the path distance between two rays, one emitted tangentially from the center of the circular

source and reaching the center of the mirror and the image plane, and a second emitted with an angle relatively to the central ray and reaching the same image position.

The path difference is expressed as:

$$\Delta F_H = (p' + d + q') - (p - d + q) \quad (19)$$

This path difference depends on $d = \rho \cdot \tan\left(\frac{\alpha}{2}\right)$.

As the parameter d depends on α , the proposed solution is to express the path difference F_H as a Taylor expansion of α :

$$\Delta F_H = C_{10}\alpha + C_{20}\alpha^2 + C_{30}\alpha^3 + C_{40}\alpha^4 + \dots \quad (20)$$

where C_{10} , C_{20} , C_{30} , and C_{40} are to the longitudinal tilt, to the longitudinal defocus, to the coma, and to the spherical aberration coefficients, respectively.

The full expression of C_{30} and C_{40} is complex, and we report the reader to the Annex of the article from Moreno (2015).

$$C_{20} \text{ (defocus)} = \frac{p^2}{2} \left[\frac{1}{p} + \frac{1}{q} - \frac{2}{R \sin(\theta)} \right] \quad (21)$$

$$C_{30} \text{ (coma)} = \frac{p^3}{4 \tan(\theta)} \left(\frac{1}{p^2} - \frac{1}{q^2} \right) - \frac{\rho}{6} \quad (22)$$

The coma coefficient is zero (for $\theta \neq \pi/2$) when:

$$q = p / \left[1 - \frac{2\rho \tan(\theta)}{3p} \right]^{1/2} \quad (23)$$

If one makes $C_{20} = C_{30} = 0$, then C_{40} becomes:

$$C_{40} \text{ (spherical aberration)} = \frac{p^4}{32 \tan^2(\theta)} \left(\frac{1}{p} + \frac{1}{q} \right) \left[\frac{p}{q} \left(\frac{3}{q} - \frac{1}{p} \right)^2 - \tan^2(\theta) \left(\frac{1}{p} - \frac{1}{q} \right)^2 \right] \quad (24)$$

where R is the radius of curvature of the mirror, p , q , θ are defined in Fig. 19.

Equation (25) has two solutions depending whether the curvatures of the mirror and the source trajectory are oriented in the same way ($\rho > 0$ and $q > p$) like in Fig. 19 or opposite ($\rho < 0$ and $q < p$).

Let us define $u = \frac{p}{q}$. By combining (23) and (24), one obtains an equation independent of the grazing incidence:

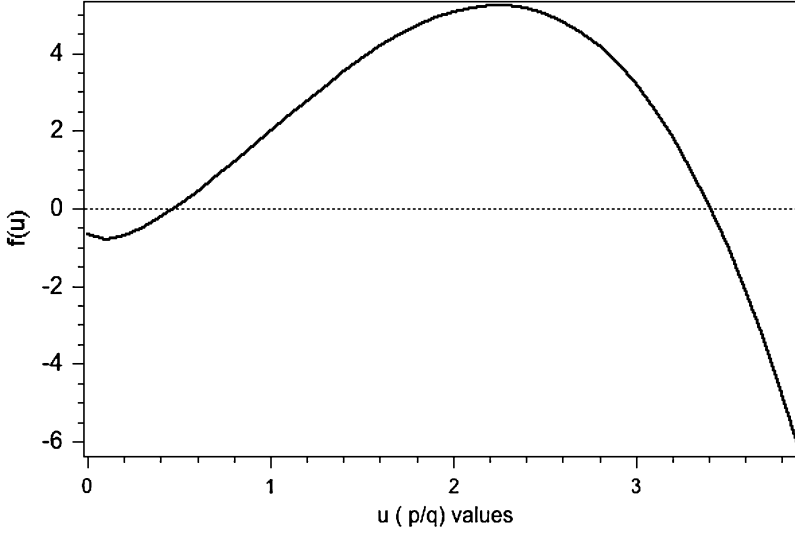


Fig. 19 $f(u)$ versus u for the case of a bending magnet radius of 4.95 m and a first distance of the cylindrical mirror to the source of 2.2 m

$$\sqrt{u}(3u - 1) - \frac{3p}{2|\rho|}(1 - u^2)(1 - u) = 0 \quad (25)$$

Equations (23), (24), and (25) are key for determining the appropriate mirror configuration, which is able to remove the horizontal source aberrations up to coefficient C_{40} included. There are two solutions depending of the source and mirror curvature orientation, $u < 1$ if the source and the mirror curvatures are oriented in the same way and $u > 1$ otherwise.

Let us illustrate the use of aberration-corrected optics, considering the following case:

At a storage ring of energy 1.9 GeV, one attends to collect infrared radiation from a bending magnet of 1.27 T (bending magnet radius of 4.99 m). Horizontal and vertical opening angle have values of 69×17 mrad².

The space constrains inside the storage ring is such that the horizontal focusing mirror (cylinder with grazing incidence angle $\neq 45^\circ$) has to be located at $p = 2.2$ m from the source.

Let us calculate q , the distance from that cylindrical mirror to the focused point, and see if the distance is compatible with the space constrains of the beamline.

From (25), one gets:

$$f(u) = \sqrt{u}(3u - 1) - \frac{3 \times 2.2}{2 \times 4.99}(1 - u^2)(1 - u) = 0$$

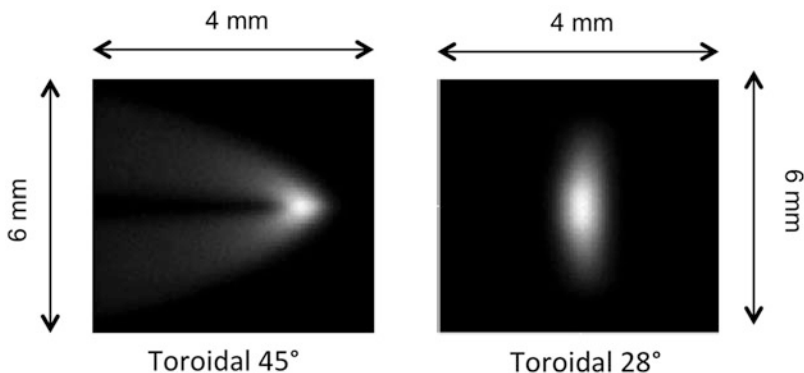


Fig. 20 First focus point profile, for a wavelength of 10 mm, considering a toroidal mirror with grazing incidence of 45° , $p = 2.2$ m, $q = 4.9$ m (left), and a toroidal mirror at the same position but with a grazing incidence angle of 28° (right). Simulation performed using SPOTX software. (Courtesy T. Moreno)

$$f(u) = \sqrt{u}(3u - 1) - 0.666(1 - u^2)(1 - u) = 0$$

The values of the $f(u)$ versus $u = \frac{p}{q}$ are reported in Fig. 19.

$f(u) = 0$ for two values of u : 0.45 and 3.4. In the present example, the source and the mirror curvature are oriented the same way, therefore <1 , therefore one has to consider the solution $u = 0.45$. This gives a value of 4.888 m for the distance of the cylindrical mirror to the focus point.

One needs now to calculate the grazing incidence angle. From $q = p / \left[1 - \frac{2\rho \tan(\theta)}{3p} \right]^{\frac{1}{2}}$, one gets $\tan(\theta) = 0.531$ and therefore $\theta = 28^\circ$.

In this example, the vertical aberration has not been corrected. The correction of such aberration is exemplified later. Since a toroidal mirror is a combination of two cylindrical mirrors, let us suppose that we have introduced a toroidal mirror with $p = 2.2$ m and $q = 4.888$ m, with the most traditional grazing incidence angle (45°) and compared the results with the grazing angle of 28° (Fig. 20).

One can clearly notice in Fig. 20 that most of the horizontal aberration has been removed with the toroidal mirror at 28° grazing incidence. Still, one can see the elongated shape of the first focus point, which is due to the vertical aberration, which has not been yet removed.

In the vertical direction, there is an overlapping of the radiation emitted all along the electronic trajectory. To remove these vertical aberrations, a cone-shaped mirror is proposed (Fig. 21).

By applying the lens equation to each ray emitted tangentially to the source, the local radius of curvature at the position where the ray reaches the mirror can be determined T. Moreno (2015):

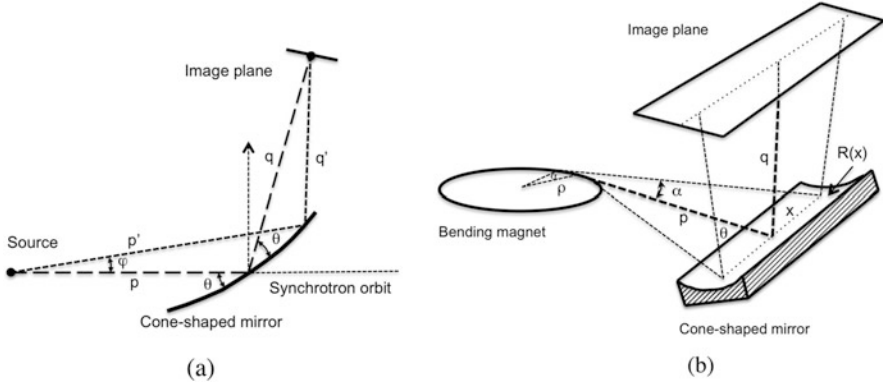


Fig. 21 Vertical source aberration scheme (left) and cone-shaped mirror schematic (right), with the parameters accounted for in the reported formula

$$R(x) = \frac{2pq}{\sin(\theta)(p+q)} \left\{ 1 - \frac{pq}{p^2(p+q)}x + \frac{1}{2p^2} \left[1 + \frac{p\rho^2(q-p)}{p^2(p+q)^2} \right] x^2 + \dots \right\} \quad (26)$$

This equation corresponds to a cone-shaped mirror, where $R(x)$ is the local radius of curvature at the position x along the mirror, p and q are the source and image distances to the center of the mirror, ρ the bending-magnet radius, and θ is the mirror grazing angle.

As for the horizontal focalization, the optical path difference is given by:

$$\Delta F_V = (p' + q') - (p + q) = C_{10}\varphi + C_{20}\varphi^2 + C_{30}\varphi^3 + C_{40}\varphi^4 \quad (27)$$

For $C_{20} = 0$, C_{30} is zero when $p = q$ or when $\theta = \frac{\pi}{2}$. For $C_{20} = 0$ and $C_{30} = 0$, the spherical aberration coefficient becomes:

$$C_{40} = \frac{p}{4 \tan^2(\theta)} \text{ if } p = q \text{ and } C_{40} = \frac{p^4}{32} \left(\frac{1}{p} + \frac{1}{q} \right) \left(\frac{1}{p^2} - \frac{1}{q^2} \right) \text{ for } \theta = \pi/2 \quad (28)$$

It has been concluded that the aberrations resulting from the vertical focusing mirror can be removed up to the comma coefficient (C_{30}), for either $p = q$ or for $\theta = \pi/2$, while, for $p = q$ and $\theta = \pi/2$, one can suppress the spherical aberration coefficient C_{40} .

In the above example, the position of polynomial mirror to remove the vertical aberration has been constrained due to the space availability of the beamline, due to the location of the various components inside the storage ring. One could only position such a mirror at 1.4 m from the source with a grazing incidence of $\pi/2$. A sagittal cylindrical mirror with $p = 1.4$ m and $q = 5.7$ m in order to fulfill the

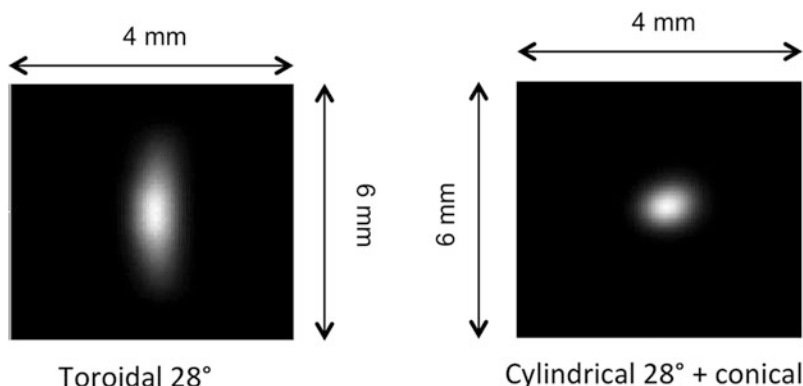


Fig. 22 First focus point profile, for a wavelength of $10\ \mu\text{m}$, considering a toroidal mirror with grazing incidence of 28° , $p = 2.2\ \text{m}$, $q = 4.9\ \text{m}$ (left), and a combination of tangential cylindrical mirror at 28° grazing incidence and a conical mirror located at $1.4\ \text{m}$ from the source (right). The optimization of the conical shape has been achieved using SPOTX software

relation $p + q = 7.1\ \text{m}$ (horizontal and vertical focusing at the first focus point) would have a radius of $R_0 = 3.179\ \text{m}$.

To compensate the vertical aberration, a conical mirror has been calculated with a radius $R_x = R_0 \pm A \cdot x \cdot R_0$. In the above example, $A = 2.04 \times 10^{-3}\ \text{mm}^{-1}$.

In Fig. 22, the profile at the first focus point of a wavelength of $10\ \mu\text{m}$ is compared to a toroidal focusing mirror at 28° grazing incidence, and with a combination of tangential cylindrical mirror and conical mirror.

Such an optical arrangement has been applied successfully, for the first time, at the Brazilian light source (Moreno et al. 2013; Freitas et al. 2018), and the optical setup is displayed on Fig. 23.

The simulated beam profile and beam propagation have been calculated and are shown in Fig. 24.

Instrumentation

Since the basic synchrotron source is spectrally “white,” nearly all applications involve a spectrometer system. The majority of such instruments are interferometers, commonly referred to as “Fourier-transform infrared” (or FTIR) spectrometers (Stuart 2004; Günzler and Gremlich 2002; Steele 2002). Commercial instruments are well-suited for use with the synchrotron source and their operation is effectively the same as for conventional thermal sources. This simplifies greatly the development and the operation of infrared synchrotron radiation beamlines. A specific note concerns the most common frequency units that are used in infrared spectroscopy. Let us recall that the velocity of light c can be expressed as:

$$c = \lambda \nu$$

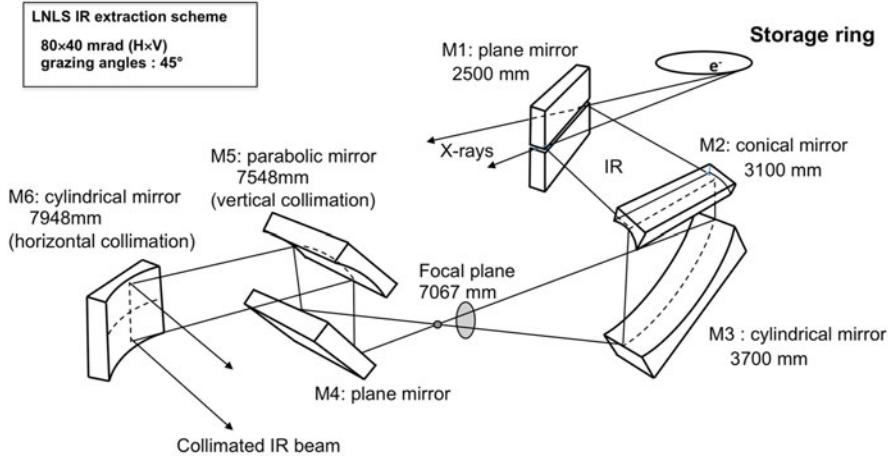


Fig. 23 Optical setup at LNLS Infrared beamline. One cylindrical mirror and one conical mirror have been calculated and optimized for producing an aberration-free beam

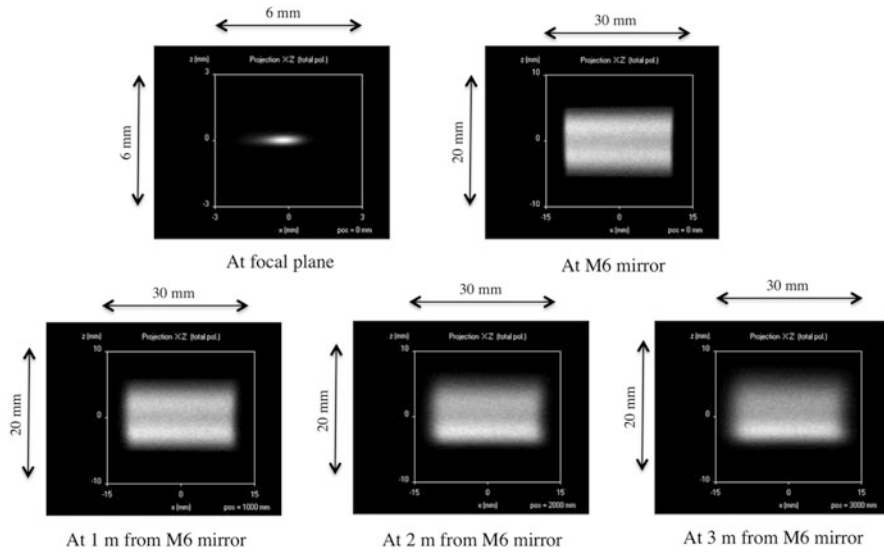


Fig. 24 Simulation of the beam profile, for a $10 \mu\text{m}$ wavelength at various position of the beamline. The beam shape is kept constant after the last cylindrical mirror (M6 – see Fig. 35) and at several meters away from this last mirror. The experimental measurements are in very satisfactory agreement with these simulations (Freitas et al. 2018; Moreno et al. 2013)

where λ is the wavelength and ν the frequency. In infrared spectroscopy, the frequency is most commonly expressed in wavenumbers (cm^{-1}), or also named inverse centimeter, which is the number of waves in a length of 1 cm $\nu = \frac{1}{\lambda}$.

This unit has the advantage of being linear with energy.

Spectrometers

For several decades, Fourier-transform infrared spectrometers have superseded the dispersive instrument and are now predominantly used as they improved the acquisition of infrared spectra dramatically.

Fourier-transform infrared (FTIR) spectroscopy (Griffiths and De Haseth 1986) is based on the interference of radiation between two beams to yield an interferogram. The latter is a signal produced as a function of the change of path length between the two beams. The two domains of distance and frequency are interconvertible by the mathematical method of Fourier transformation.

The radiation emerging from the synchrotron source is, for most of the cases, passed through an interferometer, in which a beamsplitter separating the incoming beam in two parts, one directed to a fixed mirror and one directed to a moving mirror, before recombining them. At exit of the interferometer, the beam is sent to the sample before reaching a detector. Upon amplification of the signal, in which high-frequency contributions have been eliminated by a filter, the data are converted to digital form by an analog-to-digital converter and transferred to the computer for Fourier transformation (Griffiths and De Haseth 1986; Stuart 2004).

A typical spectrometer is composed of an internal source (globar), an interferometer, a sample compartment, and one or many detectors (Fig. 25).

In most cases, an external input port allows the synchrotron beam to be substitute to the internal source.

Martin-Puplett spectrometers are also used for long wavelength studies and coherent synchrotron (Martin and Puplett 1970). The Martin-Puplett interferometer (MPI) is a differential Fourier-transform spectrometer that measures the difference between spectral brightness at two input ports. This unique feature makes the MPI an optimal zero instrument, able to detect small brightness gradients embedded in a large common background.

It is similar to a Michelson interferometer, except that the beamsplitter are wire grid polarizers, and mirrors in the beam path are rooftop mirrors to flip the polarization of the light reflecting off of them by 90°.

High spectral resolution spectrometers are mandatory instrument for recording the ro-vibrational spectra of gas phase using synchrotron infrared radiation. A long arm for the moving mirror of the interferometer achieves the high resolution, and few commercial instruments do exist. For more details, we report to the article of Quack and Merkt (2011). An improved unapodized resolution of 0.00053 cm^{-1} has been achieved at the Swiss Light Source, using a new prototype of the Bruker ETH-SLS 2009 spectrometer prototype (11-chamber system) (Quack and Merkt 2011).

Microscopes

In its typical configuration, the IR microspectrometer is an FTIR spectrometer system combined with a microscope and IR detector. Figures 26 and 27 show schematics for the two most common configurations.

Figure 26 illustrates a conventional scanning microspectrometer system where a small area (a “point”) is spectroscopically sampled by the instrument. Point spectrum is recorded and raster scanning the specimen through the focused beam

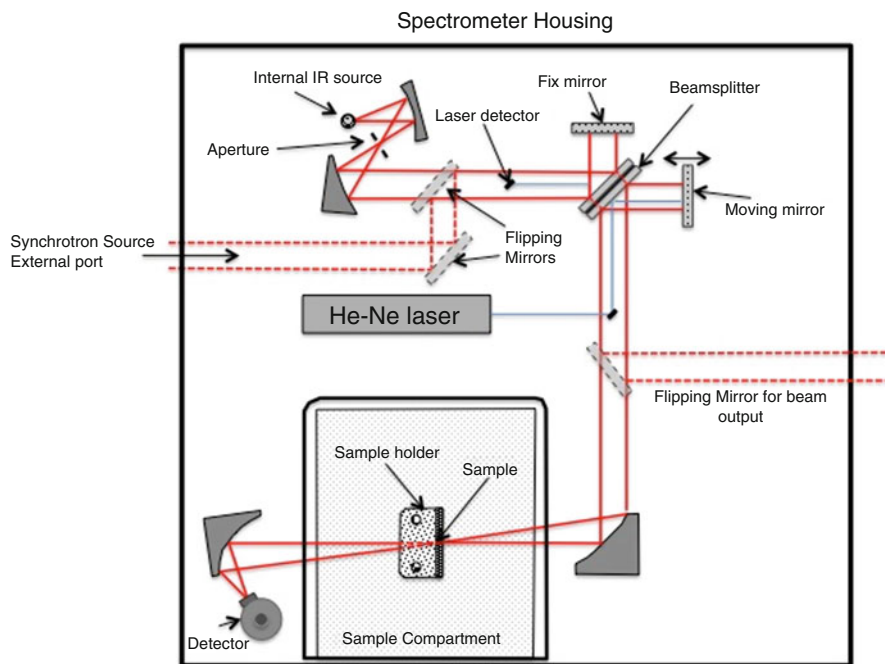


Fig. 25 Schematic of a Fourier-transform infrared spectrometer. External port is used to input the synchrotron beam. Analysis can be done inside the sample compartment, but the beam, after the interferometer, can also be directed outside for a sampling technique which requires more space, or towards an infrared microscope. In such a case, the detector is located outside the spectrometer

allows generating a chemical image. Since only a single point is sampled at a time, these instruments use a single-element detector. The microscope itself uses reflecting Schwarzschild-type objectives to avoid chromatic aberrations. An aperture can be placed at either or both of the conjugate foci for the objectives, thus constraining the illuminated or detected area on the specimen. On some microspectrometer models, the aperture on the illumination beam is called the “upper” aperture while that for the detection optic is called the “lower” aperture.

Typical magnifications range from 6X up to 50X, with 15X and 32X (36X) among the most common. Numerical apertures (NAs) vary from 0.3 up to 0.7, with a value of ~ 0.6 commonly available. In the mid-IR, these objectives deliver diffraction-limited performance over an area extending 100–200 μm from the optic axis. The design causes the central portion of the objective’s aperture to be obscured, losing up to 25% of the aperture area. This obscuration leads to significant diffraction effects when compared with a conventional microscope objective (Carr et al. 2007) (Fig. 28).

As mentioned earlier, moving the specimen through a microfocused IR beam in a raster-like fashion performs microspectroscopy imaging with a single-element

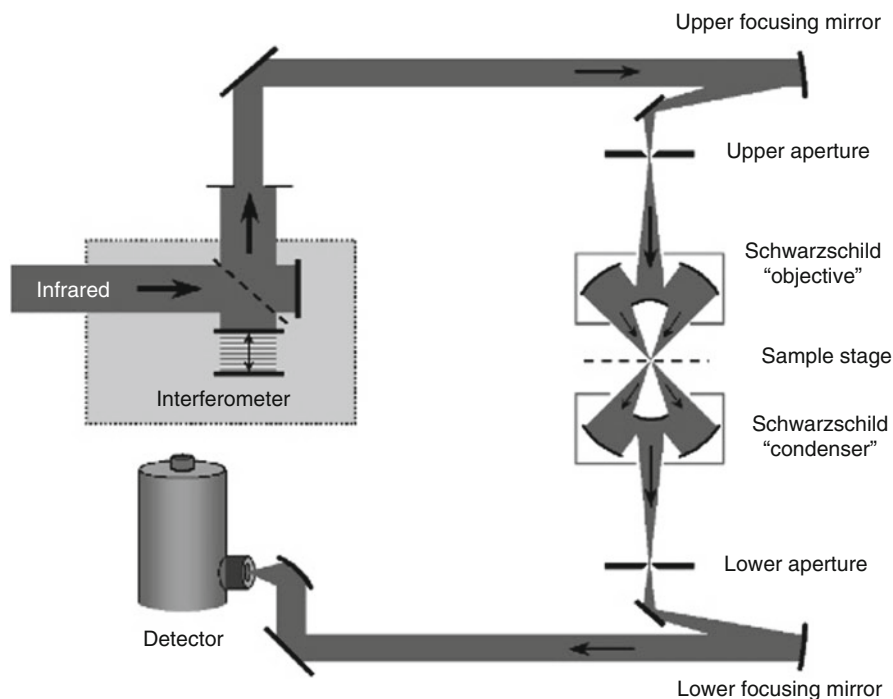


Fig. 26 Schematic for a scanning IR microspectrometer system using a single-element detector and the possibility for confocal operation where aperturing is used both before and after the sample. (Taken from Carr et al. 2007)

detector. In particular, a complete spectrum is collected individually at each point of the specimen to be imaged, with the spot size controlled by apertures and the step size usually set to have the sampled spots to somewhat overlap. Desirable characteristics of the resulting image are: (1) high signal to noise at each pixel, (2) good lateral spatial resolution, and (3) good contrast fidelity (Carr et al. 2007) (i.e., the observed change in a particular spectral intensity from point to point accurately matches the specimen's actual composition).

The spatial resolution is diffraction limited and has been discussed by Carr (2001). The measured resolving power has been shown to be in good agreement with diffraction theory, including a 30% improvement for a confocal optical arrangement. Carr (2001) has also shown that confocal setup leads to better image contrast. The diffraction limit is achieved when the instrument's apertures define a region having dimensions equal to the wavelength of interest. When in the confocal arrangement, the diffraction limit is close to $\lambda/2$.

There is a much faster process to collect spectra and to generate chemical images. By replacing the single-channel detector by a multichannel focal-plane array (FPA) detector, the spectra in a wide field of view are collected in parallel. The schematic

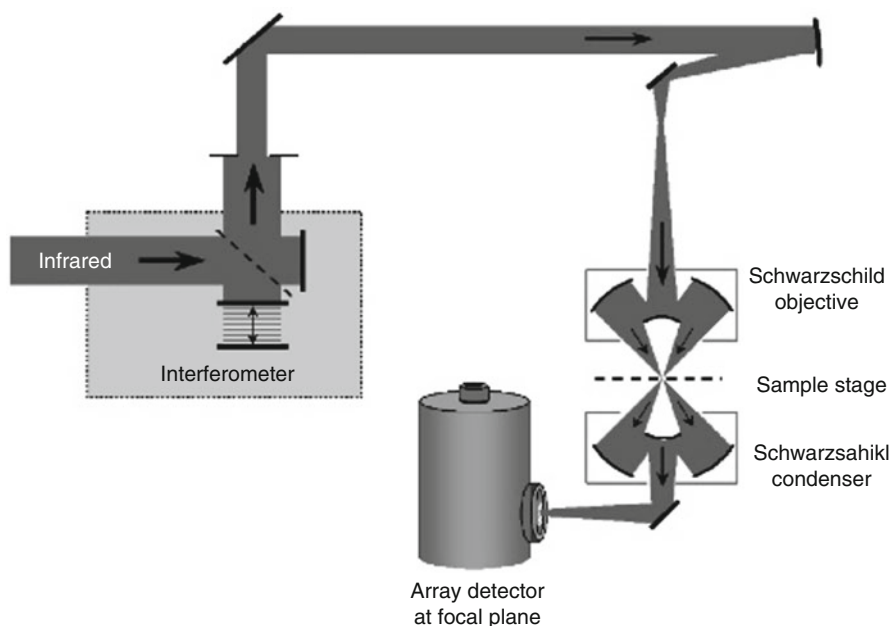


Fig. 27 Schematic for an imaging IR microspectrometer system using an FPA detection system. Note that the “upper” aperture must be left “open” or removed to allow light to fall onto the entire area to be imaged. (Taken from Carr et al. 2007)

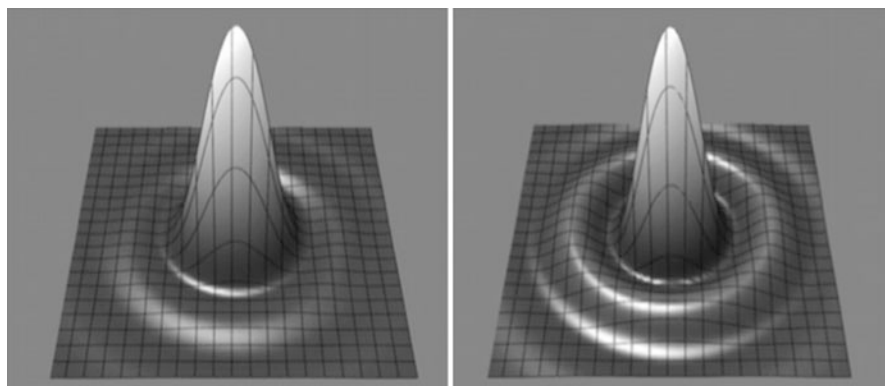


Fig. 28 Calculated intensity profiles for a simple, full aperture objective (Airy pattern, left) and a Schwarzschild objective with central obscuration (right). The same NA and wavelength were used for both calculations. Note the large first-order diffraction ring for the Schwarzschild objective. (Taken from Carr et al. 2007)

in Fig. 28 shows a simplified layout for an IR microspectrometer based on a staring-type FPA detection system. The system also uses Schwarzschild objectives, but the apertures for constraining the microscope’s sensitive location are left open, that is,

they do not provide any spatial discrimination. Thus, the microscope's first objective illuminates a rather large area, and this illuminated region is then imaged onto the FPA detector by the second Schwarzschild objective. Spatial discrimination is provided by the individual pixels of the detector, each one serving as its own "aperture." Because there is no matching aperture for the illumination objective, this system does not meet the confocal definition. Though the images obtained with FPA systems are of high quality, there is not an exact representation of the specimen's properties. Instead, the images are degraded due to limitations of the optical system and other factors (detector fidelity, phase correction, apodization, etc.) (Carr et al. 2007). The most significant limitation for high spatial resolution imaging, however, is the diffraction of light, and it is discussed in more details in Carr et al. (2007).

Detectors

An extensive article about infrared detectors, their composition, and their performances in various photon energy domains has been reported by A. Rogalski (2002, 2003).

The increased sensitivity, resolution in system complexity of FPAs offer significant advantages in military as well as civilian applications in thermal imaging, guidance, reconnaissance, surveillance, ranging, and communication systems. From fundamental considerations, HgCdTe is the most important semiconductor alloy system for IR detectors in the spectral range between 1 and 25 μm . HgCdTe detectors as the intrinsic photon detectors absorb the IR radiation across the fundamental energy gap and are characterized by high optical absorption coefficient and quantum efficiency and relatively low thermal generation rate compared to extrinsic detectors, silicide Schottky barriers, and QWIPs.

Detectivity D^* is the main parameter characterizing normalized signal to noise performance of detectors, and more details can be found in the article of Rogalski (2003).

The detectivity of several infrared detectors is reported in Fig. 29.

In synchrotron infrared facilities, especially for the mid-to-near infrared region, the most widely used detector is HgCdTe, with a broadband or narrow band frequency, even though, for some applications, a combination of InSb and HgCdTe – narrow band detectors provide a highest sensitivity.

The long wavelength region, also called most commonly far infrared or THz, requires specific detectors named bolometers. They are mainly composed of composite silicon systems that are housed in a liquid helium dewar with a liquid nitrogen-cooled radiation shield. Such detectors are very sensitive to thermal radiation and are predominantly used in the infrared spectrum between 10 and 5000 μm (30 THz to 60 GHz). Such extremely sensitive thermistor is cooled to liquid helium temperatures in order to decrease the thermal background. A temperature change of the detector occurs when a thermal radiation reaches it. This results in a marked change in the resistance, and, with the applied bias current, a voltage difference is detected.

Being a thermal sensor, the time constant of such bolometer is in the order of milliseconds.

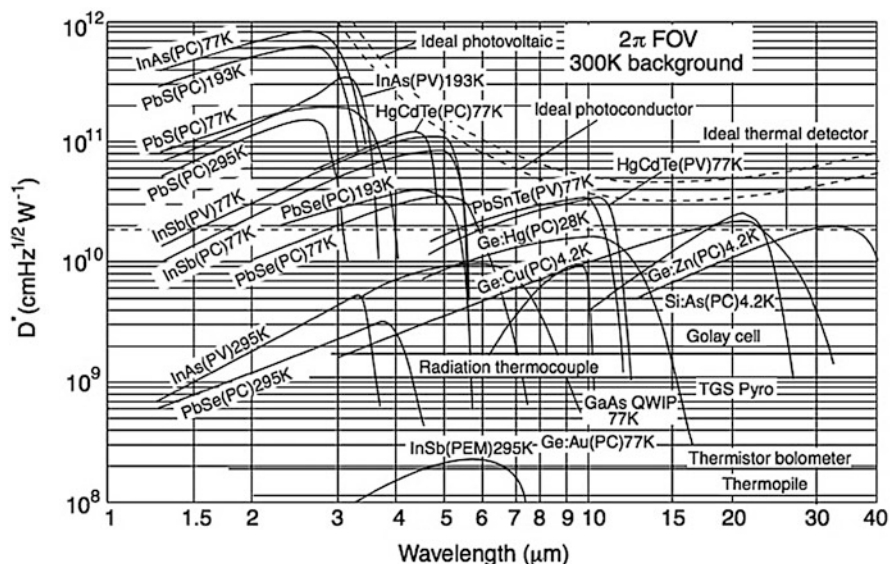


Fig. 29 Comparison of the D^* of various commercially available infrared detectors when operated at the indicated temperature. Chopping frequency is 1000 Hz for all detectors except the thermopile (10 Hz), thermocouple (10 Hz), thermistor bolometer (10 Hz), Golay cell (10 Hz), and pyroelectric detector (10 Hz). Each detector is assumed to view a hemispherical surrounding at a temperature of 300 K. Theoretical curves for the background-limited D^* (dashed lines) for ideal photovoltaic and photoconductive detectors and thermal detectors are also shown. *PC* photoconductive detector, *PV* photovoltaic detector, *PEM* photoelectromagnetic detector. (From Rogalski (2003) with permission)

The doped silicon bolometer (germanium-doped bolometer are also used) is an extrinsic detector, and the doping element determines its spectral response (Norton 1991; Rogalski 2003).

Superconducting hot electron bolometers have faster time constant (Shurakov and Lobanov 2015) and are used in some facilities.

Beyond the Diffraction Limit: Towards Nanospectroscopy

The chemical specificity that FTIR techniques allow is powerful and a challenge has been to bring this power to the nanometer scale well beyond the diffraction limit. This ability to simultaneously have nanoscale spatial resolution and chemical specificity will allow us to gain fundamental insights into natural and engineered heterogeneous materials and systems.

The fundamental properties of life occur at the nanoscale where chemical signals and macromolecular conformational changes are ultimately in charge of how life progresses at the whole organism level across the biosphere. Similarly, nanoscale differences engineered into materials can change critical parameters in charge of superconductivity, band gaps, magnetism, and other key macroscopic uses of these materials. And the nanoscale porosity of naturally occurring minerals greatly affects

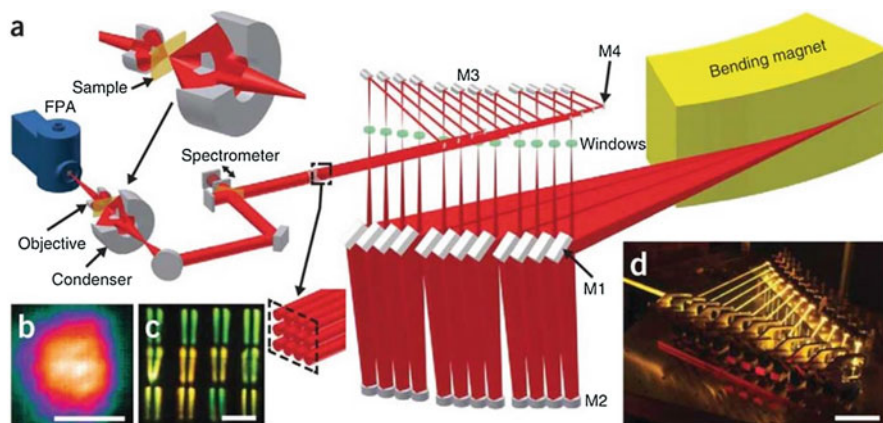


Fig. 30 (a) Schematic of the IRENI setup. M1–M4 are mirror sets. (b) A full 128×128 pixel FPA image with 12 overlapping beams illuminating an area of $\sim 50 \mu\text{m} \times 50 \mu\text{m}$. Scale bar, $40 \mu\text{m}$. (c) A visible-light photograph of the 12 beams projected on a screen in the beam path (dashed box in a). Scale bar, 1.5 cm. We display the beams as one beam from then on in the schematics. Each beam exhibits a shadow cast by a cooling tube upstream, which is not shown in (a). (d) Long-exposure photograph showing the combination of the 12 individual beams into the beam bundle by mirrors M3 and M4. Scale bar, 20 cm (Nasse et al. 2011)

their properties in the sub-earth environment and play important roles related to oil and gas extraction and carbon sequestration.

Here we describe various developments that beat the diffraction limit while using the high brightness advantages of a synchrotron IR source to push the frontiers of imaging science. Later in this chapter, we cover some exciting scientific applications enabled by these technical developments.

Array Detector Imaging and Oversampling

Recently, the development of commercially available focal-plane array (FPA) detectors has enabled rapid FTIR imaging over larger fields of view. This was exploited in the IRENI beamline setup at the SRC by using 12 synchrotron IR beams to fully cover the entire array and enable high s/n imaging with fields of view greater than $100 \times 100 \mu\text{m}^2$ (Nasse et al. 2011) (Fig. 30).

The use of an FPA detector also allows using higher numerical apertures in the IR microscope to yield a projected pixel resolution of less than $1 \times 1 \mu\text{m}^2$, which is beyond the diffraction limit for all mid-IR wavelengths. Use of a measured point spread function (PSF) and deconvolution of an image acquired with oversampled resolution allows a marginal improvement in resolution beyond the Abbe limit (Mattson et al. 2012; Stavitski et al. 2013). Figure 31 shows the resolution enhancement achieved on test samples at IRENI (Mattson et al. 2012), and Fig. 32 shows a biological tissue samples imaged with an FPA illuminated with four beams at the NSLS from reference (Stavitski et al. 2013).

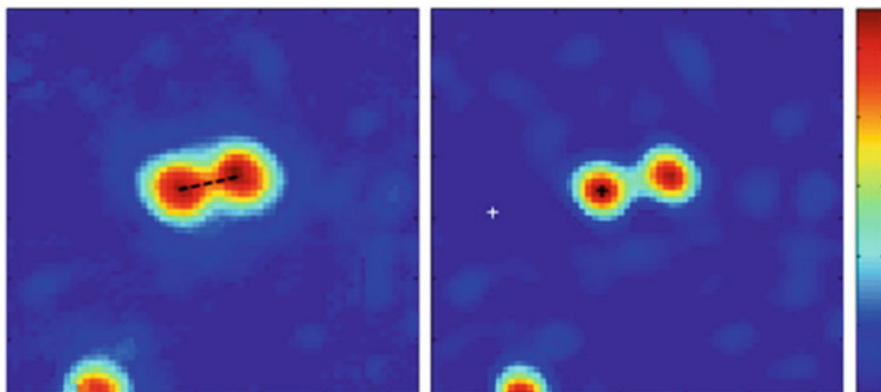


Fig. 31 Three polystyrene beads dispersed in a 10 micron thick polyurethane film imaged with the IRENI beamline. On the left is the original unprocessed image of the 3020 cm^{-1} aromatic CH stretching peak showing two beads close together and a third near the bottom of the image. Right image is the deconvoluted image showing clearly better spatial resolution. (From Mattson et al. 2012)

Scanning Probe Systems

The combination of scanning probe systems such as atomic force microscopy (AFM), which have tip-based imaging resolutions in the nanometer scale based on the physical size of the tips, with the chemometric process of synchrotron-based FTIR spectroscopy is a powerful combination and new imaging and spectroscopy modality on a truly nanometer scale. There have been several approaches to accomplish this combination. One that has worked particularly well with the broad spectral bandwidth and high brightness of a synchrotron IR source is scattering-type scanning near-field optical microscopy, s-SNOM.

In s-SNOM, free space IR light is focused and scattered by typically a metallic AFM tip and is detected in the far field with a standard IR detector. This technique provides spatial resolution equivalent to the tip apex radius, often around 10 nm, independent of the wavelength of light (Knoll and Keilmann 1999; Keilmann and Hillenbrand 2004; Muller et al. 2015). Therefore, it works in the microwave, IR, and visible by using appropriate tip materials.

Another technique uses photothermal imaging in the near field and is known as AFM-IR. It provides a direct coupling of the thermal absorption of the incoming IR light pulse and an AFM tip measures the amount of thermal expansion (Dazzi et al. 2005). The spatial resolution of this technique is tied to both the tip apex size and the thermal diffusions within the sample, so it is typically better than 100 nm (Feng et al. 2014).

These new scanning probe methods improve the spatial resolution of infrared imaging and spectroscopy by 100- to 1000-fold beyond the diffraction limit. The signals from these nanoscale techniques, however, are weak with large backgrounds that need suppression, and therefore, these near-field techniques are often limited

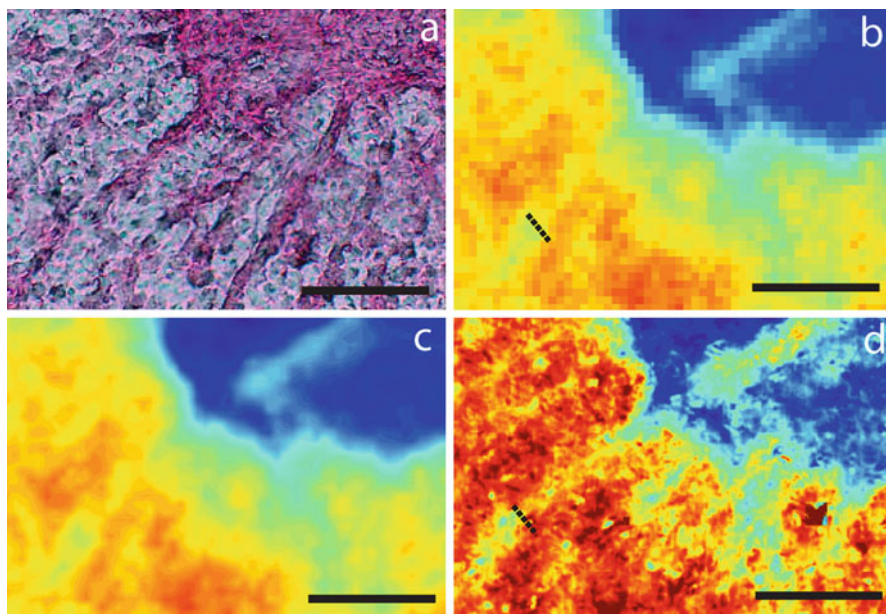


Fig. 32 FTIR imaging with a globar versus multiple synchrotron beams. (a) Optical micrograph of the mouse spinal cord cross section stained with eosin Y. Scale bar is 100 μm . (b) FTIR images showing the ratio of integrated absorbance for the C–H stretch ($3000\text{--}2800\text{ cm}^{-1}$) spectral regions acquired with the globar and linear array detector ($6.25 \times 6.25\text{ }\mu\text{m}$ size); (c) the same data set as in panel (b) interpolated onto a mesh with $0.54\text{ }\mu\text{m}$ spacing; and (d) same area scanned using synchrotron and FPA instrument ($0.54 \times 0.54\text{ }\mu\text{m}$ pixel size) showing much more fidelity. Note that panels (b–d) are plotted on the same color scale. (From Stavitski et al. 2013)

by the IR source characteristics. For broadband infrared spectroscopy covering a typical mid-IR FTIR spectrometer spectral range, the high brightness of a synchrotron IR beamline enables these near-field techniques to be truly broadband spectral tools providing chemical insights at the nanometer scale.

Synchrotron IR light and near-field probes have a history. In 2002, SR IR light was first coupled to an photothermal probe of a specially designed AFM head in Daresbury in England (Bozec et al. 2002). They saw improved spectral contrast on a polypropylene/polycarbonate sample compared to with a thermal IR source. In 2004, Schade et al. (2004) demonstrated near-field THz spectroscopy and imaging using CSR at the BESSY synchrotron in Germany. They were able to achieve $\lambda/12$ at 12 cm^{-1} and performed imaging of biological tissues with this sub-diffraction resolution (Schade et al. 2005). These measurements pioneered going beyond the diffraction limit and demonstrated that the design of the probe was important to obtain sufficient signal throughput. In 2012, Ikemoto et al. (2012) achieved 300 nm resolution at 1000 cm^{-1} on a gold/silicon test structure using a scattering type near-field setup, s-SNOM. In 2013, Hermann et al. (2013) used the Metrology Light Source in Germany with an asymmetric Michelson interferometer and a

commercial s-SNOM instrument (Neaspec GmbH) to achieve better than 100 nm spatial resolution. Also in 2013, D'Archangel et al. (2013) used the Advanced Light Source to measure metastructures with better than 100 nm spatial resolution using a modified Veeco/Bruker Innova AFM. After incorporating a commercial FTIR (Thermo-Scientific) with this AFM, custom modified to run in asymmetric Michelson configuration, Bechtel et al. demonstrated in 2014 (Bechtel et al. 2014b) a spatial resolution of better than 40 nm and coined the term synchrotron infrared nano-spectroscopy (SINS).

Near-field IR techniques have been demonstrated more recently at Synchrotron SOLEIL (Peragut et al. 2014) at the Brazilian Synchrotron Light Laboratory (LNLS) (Pollard et al. 2016; Freitas et al. 2017) and is planned for several more synchrotron facilities worldwide.

Figure 33 shows a generic schematic of a SINS experimental setup and has been implemented with commercial instruments (Hermann et al. 2013; Freitas et al. 2018) or by customizing individual components (Bechtel et al. 2014a). In SINS, the incident synchrotron IR light is focused onto a conductive AFM tip which is in tapping mode in nanometer proximity to the sample. The conductive tip effectively acts as an optical antenna and its nanoscale tip apex becomes the source of scattering the light from the far field into the sample and back out. To first approximation, the spatial resolution of the technique is independent of wavelength and is only limited by the tip apex radius, which can be <10 nm.

In order to suppress the large background signal created by the light reflecting and scattering off of the rest of the tip and sample structure and pull out the desired but weaker signal coming from just the tip apex region, a modulation technique is used. By running the AFM in tapping mode, or noncontact mode, the tip resonantly moves in and out of near-field distance from the sample. The near-field interaction is highly nonlinear, which means that demodulation using a lock-in amplifier at higher

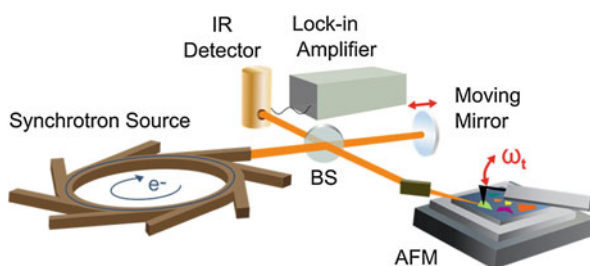


Fig. 33 A schematic of a SINS experiment. Synchrotron light from an IR beamline enters an asymmetric Michelson interferometer where a beamsplitter (BS) directs half of the light to the tip of an AFM and the other half to the moving mirror. The light scattered back from the tip is recombined with the light from the moving mirror at the beamsplitter and is then sent to the IR detector. A lock-in amplifier demodulates the signal using a harmonic of the tapping frequency, ω_t . Resultant interferograms as a function of moving mirror position can be converted into the real and imaginary parts of the sample spectrum

harmonic frequencies of the tapping frequency (for example, $2\omega_t$, $3\omega_t$, etc.), will greatly enhance the near-field contrast, albeit at the expense of total signal strength.

Secondly, by placing the s-SNOM setup within an asymmetrical Michelson interferometer setup, one benefits from heterodyne amplification of the weaker scattered near-field signal with the stronger reference arm beam (Huth et al. 2011, 2012). The self-homodyne signal is constant for a single AFM tip position, so by AC coupling via modulating the tip to sample distance in tapping mode, this self-homodyne signal is removed and the result is an interferogram that can be Fourier-transformed to obtain the complex near-field spectrum. The asymmetric configuration allows determination of both the amplitude and phase components of the sample response. For molecular resonances, the amplitude response shows dispersive lineshapes, whereas the phase response yields Lorentzian-like lineshapes. By properly modeling the tip-sample interaction, one can extract the complete dielectric response without the need for Kramers-Kronig transformations (McLeod et al. 2014; Govyadinov et al. 2013; Cvitkovic et al. 2007). To a good approximation, the imaginary component of the scattered signal, $\text{Im}[\sigma]$, is proportional to the absorption coefficient of thin molecular films (Huth et al. 2012), meaning they can be directly compared to far-field transmission spectra including FTIR spectral libraries.

The spectral range that is covered by a SINS experiment is limited by the choice of beamsplitter and detector, not the source since synchrotron bend magnets cover from the far-IR to the x-ray. Most mid-IR applications use a germanium-coated KBr or ZnSe beamsplitter that have low-frequency cutoffs around 400 and 500 cm^{-1} , respectively. An MCT photoconductive detector with a low-frequency cutoff around 750 cm^{-1} gives the highest sensitivity, but a lower sensitivity wide-band MCT can be employed to reach to 500 cm^{-1} .

For far-IR measurements, a different beamsplitter and detector combination must be employed. Beamsplitters made of KRS-5 can extend the spectral coverage down to about 200 cm^{-1} , and a Si beamsplitter can work down to around 10 cm^{-1} . Typical far-IR detectors, such as liquid helium-cooled bolometers, typically have to slow a response time (bandwidths around 1 KHz) to respond to the tip modulation frequencies used in SINS. Khatib et al. (2018) has demonstrated using a liquid helium-cooled Ge:Cu detector with a low-frequency cutoff around 330 cm^{-1} (Fig. 34). Other impurity-doped germanium detectors and advances in speeding up bolometer response times offer the possibility of extending the range further into the far-IR.

Applications

Spectroscopy Using Coherent Radiation

Coherent synchrotron radiation (CSR) has opened up the ability to perform measurements within the so-called THz-gap using this novel high-power THz and sub-THz source (Carr et al. 2002; Abo-Bakr et al. 2002, 2003). Several facilities

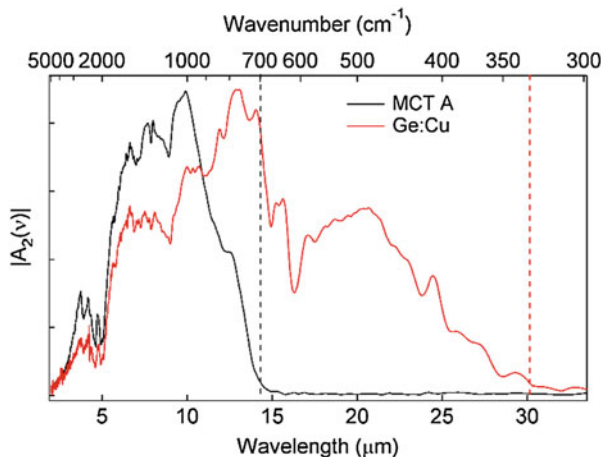


Fig. 34 The measure second harmonic signal in a SINS setup at the ALS with a typical mid-IR setup (black line) and an extended far-IR choice of detector and beamsplitter (red line). The intensities are normalized. (From Khatib et al. 2018)

now offer a few days a year where the accelerator is run in a mode to specifically produce the short electron bunches required for CSR. One scientific area where this has been specifically exploited is the low-frequency study of novel superconductors, even though the initial use spread over solid state and biology (Basov et al. 2004). A high-flux synchrotron source allows a high accuracy in the detection of small effects in the reflectivity spectra and overcomes the problem of the very low intensity transmitted by these systems. The reflectivity of such samples were measured in the traditionally difficult sub-THz region and fit to a BCS model like on cuprate high-temperature superconductor (Singley et al. 2004), V_3Si (Calvani et al. 2008; Perucchi et al. 2010).

THz has potential to become a supplemental method to imaging methods for granular media (Born and Holldack 2017) and Fourier-transform THz-EPR (Nehrkorn et al. 2017).

Frequency combs potential with coherent synchrotron radiation has been recently demonstrated and applied for the study of pure rotation transitions in acetonitrile (Tammaro et al. 2015).

Spectroscopy Using Noncoherent Far-IR Synchrotron Radiation

Solid-State Physics

Synchrotron infrared beamlines have been used for studying a number of exciting condensed matter systems from high-temperature superconductors, to VO_2 , to semiconductors, to graphene.

Several studies have been carried out and are ongoing in facility where the far-IR capabilities is thoroughly exploited by appropriate detectors, spectrometers (and beamsplitters), and sample environment. Example is the terahertz reflectivity measurements on SrTiO₃ crystals (Nucara et al. 2016) and the determination of a band structure asymmetry of bilayer graphene (Li et al. 2009).

Optical conductivity has been studied using far-infrared (ThZ) synchrotron reflectivity (Lo Vecchio et al. 2014; Autore et al. 2014; Mirri et al. 2012; Pellicer-Porres et al. 2011, 2013) among others. There exists a vast literature of the far-IR spectroscopy for solid-state physics.

Gas Phase

Among the first application of the synchrotron brightness advantage, high spatial resolution spectroscopy of condensed-phase samples was exploited. Max-Lab in Sweden (Nelander and Sablinskas 1995; Nelander 1993) and LURE in France (Roy et al. 1993) pioneered high-resolution gas-phase IR spectroscopy, since the highly collimated source provides a marked advantage for high-resolution spectroscopy. The synchrotron source has been found to replaces the usual thermal source in a Fourier-transform IR spectrometer, giving an increase of up to two (or even more) orders of magnitude in signal at very high resolution. This is because Fourier-transform spectrometers which are based on the Michelson interferometer principle need smaller entrance apertures for higher resolution, just as grating spectrometers need narrower slits.

The quality of a spectrum depends on the spectrometer, not the source, and it is already possible to obtain excellent results using conventional thermal sources. It is worst noting that excellent results can be obtained using specifically dedicated spectrometer (very long travelling distance of the moving arm of the interferometer) only for much higher resolution ($\leq 0.004 \text{ cm}^{-1}$), and it is only at very high resolution that the synchrotron source becomes really advantageous. For most infrared spectroscopy, the achievable resolution is limited by the Doppler width of the sample molecules being studied.

Three facilities have dedicated gas-phase infrared beamlines: Canadian Light Source (May 2004), Australian Synchrotron (Creagh et al. 2006), and SOLEIL (Roy et al. 2006).

McKellar has summarized the advantage of using the synchrotron source for high resolution spectroscopy in gas phase, as well as the most important highlights in this field in a recent article (McKellar 2010).

Several gas cells are made available at infrared synchrotron high-resolution stations and are constant upgraded; for example, an elegant cryogenic long path cell with variable optical path length cells (Kwabia Tchana et al. 2013) and temperature regulated around 165 K. Doppler-limited spectra of SF₆ Nu₃ + Nu₅ combination band have been recently obtained (Faye et al. 2018), supersonic jet experiments (Georges et al. 2017; Cirtog et al. 2011).

Surface Science

Bonding between adsorbed molecules and substrates has been at the heart of the identified potential of far-IR spectroscopy using the synchrotron source. Most of the vibrational bands associated with these bondings lie in the far-IR region of the electromagnetic spectrum. In this region, accessing such informations was very difficult (Engström and Ryberg 2001) due to the weakness of the thermal source and its low brightness, since, in order to amplify the electric field at the surface of the metallic substrate, a grazing incidence geometry is mandatory.

The main initial objective at the beginning of the exploitation of the synchrotron far-infrared photons was to study the bonding between adsorbates and substrate (mainly metallic). Thorough studies have been performed on Cu and Pt surfaces (Hirschmugl et al. 1990; Dumas et al. 1997; Surman et al. 2002; Baily et al. 2003). Other studies identified the bonding nature of organic molecules on metallic surface (Humblot et al. 2003).

Vibrational dynamic studies are possible only by using the synchrotron source. At the beginning of the 1990s, the interest of the study of the low energy modes was renewed when Persson suggested that frustrated translational modes of molecules or atoms are the key to the frictional force induced by the adsorbate on the metallic surface (Persson and Volokitin 1994). A direct relation with resistivity change was suggested and verified experimentally with the synchrotron far-infrared source, by simultaneous measurements of d.c. resistivity and IR reflectivity changes on the CO/Cu system (Hein et al. 1999, 2000; Dumas et al. 1999).

Today, there is no beamline dedicated to surface science, and the motivation has been lost for such exciting research field.

Microscopy at Limited Diffraction Spot Size

Material Science

Some interesting ways in which the properties of infrared synchrotron radiation have been used for studying samples important to solid-state physics, materials science, catalysis, and soft matter such as polymer science has been reviewed in Martin and Dumas (2012). Since then, materials science research continues to be a strong player both pushing technical developments and generating exciting and high-profile results, not only in microscopy but also in nanospectroscopy.

Extremes Conditions

High-pressure synchrotron IR spectromicroscopy represents an ideal coupling of diamond anvil cells (DAC) and IR radiation in the entire spectral region (THz to mid-IR) for spectroscopic studies under extreme conditions such as static and dynamic compression and at variable temperatures. Several examples can be found in Martin and Dumas (2012).

Earth and Planetary Science

Synchrotron infrared Fourier-transform infrared microspectroscopy has provided paramount information regarding the molecular structure of organic and inorganic components for chemical characterization of geological samples, being, in addition nondestructive for the characterization of minute microfossils, small fluid and melt inclusions within crystals, and volatiles in glasses and minerals.

SR FTIR examination of the interplanetary dust particles has demonstrated its ability to detect organic matter in small particles within picokeystones from the Stardust interstellar dust collector (Bechtel et al. 2014a; Martin et al. 2010).

Archaeology

The study of cultural heritage and archaeological materials has benefited a lot from the synchrotron infrared microscopy. The range of materials that have been studied is very broad, ranging from painting materials, stone, glass, ceramics, metals, cellulosic and wooden materials in relation with the diversity of samples found at archaeological sites, museums, historical buildings, etc. The main objectives were the study of the alteration and corrosion processes, the understanding of the technologies and identification of the raw materials used to produce archaeological artifacts and art objects, and the investigation conservation and restoration practices (Bertrand et al. 2012; Cotte et al. 2009; Salvadó et al. 2005).

Biology

Biology and biomedical studies represent the most important user community at many infrared beamlines (more than 50% on average).

The high spatial resolution and higher spectral quality have brought a lot of interest for single cells, tissues, and subcellular imaging in biology. In addition, the synchrotron infrared beam induces a negligible sample heating and opens the way of in-vivo studies, without the beam damage issue faced with X-rays beam (Martin et al. 2001).

Beyond the determination of atomic resolution structures, there is the daunting task of understanding how macromolecules assemble and function inside a living cell, where thousands are simultaneously interacting in a complex biochemical environment. Infrared spectroscopy has been identified as one of the key approaches for this field of “functional biology.” Based on the relevant biomarkers, there are a lot of information contained in FTIR spectra: protein secondary structure - Amide I ($1600\text{--}1700\text{ cm}^{-1}$) and Amide II ($1500\text{--}1560\text{ cm}^{-1}$), features arise primarily from the C–O and C–N stretching vibrations of the peptide backbone, respectively. The infrared signature of the protein has been shown to be particularly sensitive to protein secondary structure based on the vibrational frequency of the Amide I (C=O) band, which is affected by different hydrogen-bonding environments for α -helix, β -sheet, turn, and unordered structures (for a review, see Miller and Dumas 2010). In addition to protein structure, FTIR simultaneously provides information about sample biochemistry, with predominant absorption features of the lipid spectrum (region $2800\text{--}3000\text{ cm}^{-1}$), ester C=O groups in the lipid (strong band at 1736 cm^{-1}), and nucleic acid spectra have C–O stretching vibrations

from the purine (1717 cm^{-1}) and pyrimidine (1666 cm^{-1}) bases. In addition, the region between 1000 and 1500 cm^{-1} contains contributions from PO_2 stretching (symmetric and antisymmetric) vibrations.

Because FTIR microspectroscopy monitors the global biochemical composition in the probed volume (i.e., tens of cubic microns), the vibrational signatures recorded are a superposition of the spectra of thousands of constituents. Yet despite the complexity, it has been demonstrated that the technique is highly sensitive to slight changes in the composition. The interpretation of these composite spectra requires sophisticated data analysis, which is still evolving through the continued development of multivariate methods. These approaches are based on the principle that there exist small but reproducible changes in the spectra that can be associated with the variations in sample properties that are investigated. There are several known statistical approaches for infrared data analysis but perhaps the most frequently used is principal components analysis (PCA).

There has been numerous applications of synchrotron infrared microscopy in Biology (Miller and Dumas 2010), including studies of biological samples in situ (Vaccari et al. 2012; Mitri et al. 2014; Loutharback et al. 2016).

Nanospectroscopy and Imaging

SINS is broadly applicable to a wide range of sample spanning scientific disciplines just like far-field FTIR with a synchrotron IR beamline. The only additional constraint is the sample must be suitable for an AFM, meaning relatively flat, and that the measurements are confined to near-surface probing. Even though SINS is a relatively new technique, the number of users working with it is rapidly growing, so at the time of this review's publication, there will already be a number of new publications and results beyond what is covered here. Since it is an emerging field, we detail hereafter examples of science being done with SINS including plasmonics, nanoparticles, biopolymers, semiconductors, electrochemistry, biominerals, and space sciences.

Bechtel et al. (Bechtel et al. 2014a) measured the phonon modes of calcium carbonate polymorphs in natural biomineral specimens, as shown in Fig. 35. And in Fig. 36, the symmetric and antisymmetric phonon modes of LiFePO_4 (LPF) and FePO_4 (FP) single microcrystals are studied to show the changes due to lithiation and delithiation of this Li-ion battery cathode material. The broad spectral coverage of SINS in both of these examples shows how the phonon modes can be followed and studied with nanoscale spatial resolution.

Liu et al. (2015) have used SINS and laser-based s-SNOM to study a number of VO_2 samples in crystalline and thin film form. By measuring the spectroscopic signatures of VO_2 phonon modes at 20 nm resolution, they were able to map our lattice and electronic changes that occur during the metal-to-insulator phase transition that is triggered via heat or mechanical strain. In a VO_2/TiO_2 film,

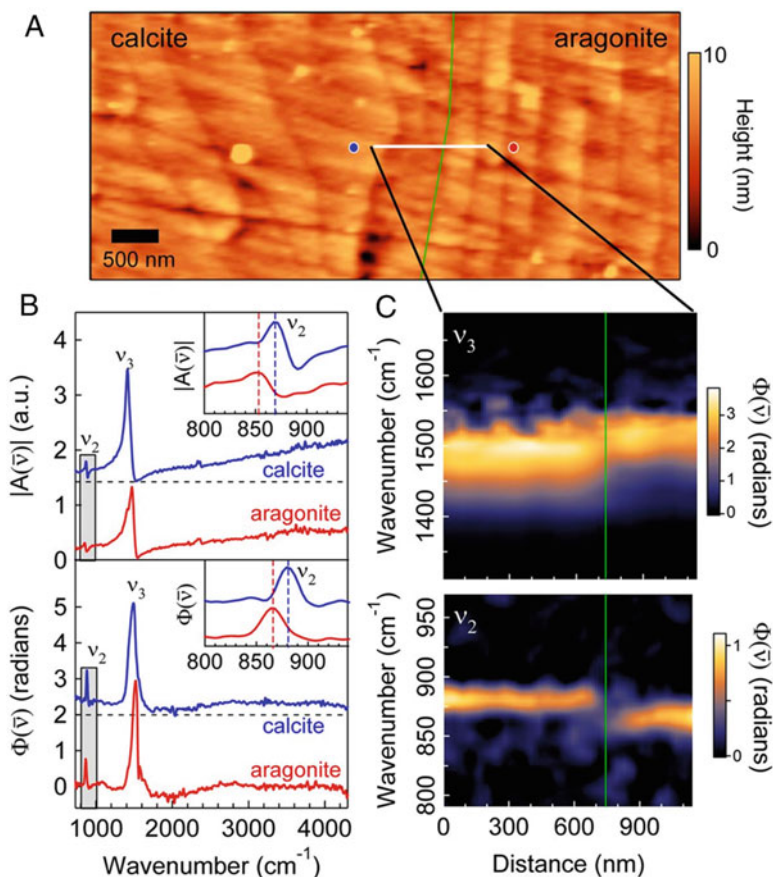
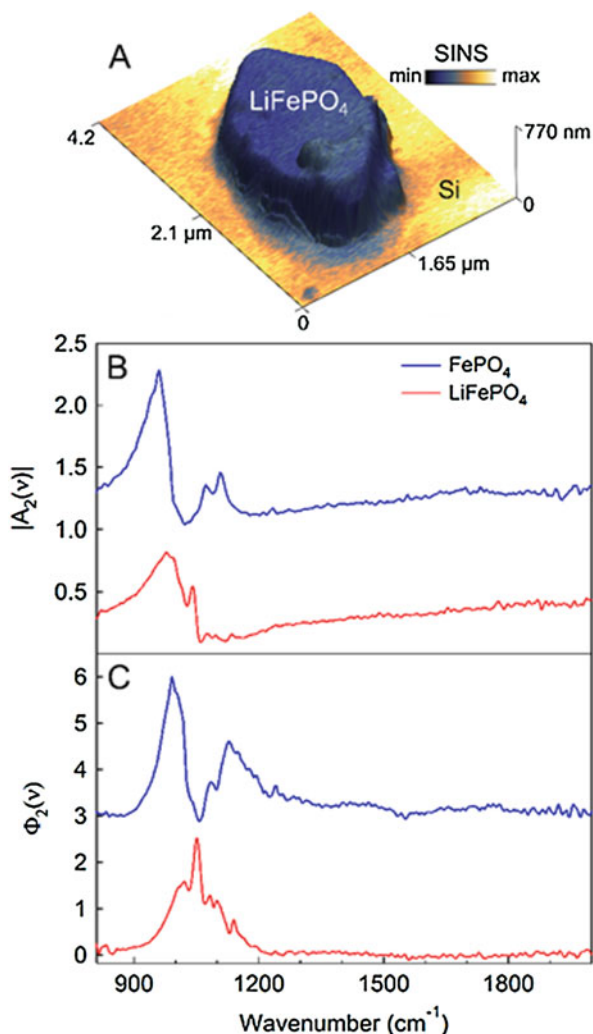


Fig. 35 Phonon mode shifts between different polymorphs of calcium carbonate are clearly visible in a line scan obtained across the transition point in this natural biomineral shell sample. (From Bechtel et al. 2014b)

they observed a red shift of the M1 phonon at 540 cm^{-1} which correlates with compressive strain along the c-axis.

Plasma polaritons and phonon polaritons are quasiparticles that can be excited by the IR light scattered off the AFM tip. Dai et al. (2014) has demonstrated with laser-based s-SNOM that the momentum provided by the confined light field at the apex of the tip will optically excite phonon polaritons in hexagonal boron nitride (hBN), which has also been seen in graphene (Fei et al. 2012; Chen et al. 2012; Gerber et al. 2014). Shi et al. (2015) have used SINS to investigate both in-plane and out-of-plane phonon modes in hBN flakes, Fig. 37. Although both modes show signs of the phonon polariton as a function of wavelength, the sign is reversed. This is consistent with the lower-frequency hyperbolic mode being of Type I whereas the higher frequency mode is Type II.

Fig. 36 LFP and FP microcrystal showing distinct spectral changes of the phonons associated with Li intercalation into and out of this Li-ion battery cathode material



Single nanoparticles can now be individually measured, thanks to the high spatial resolution of SINS. Johns et al. (2016) and Runnerstrom et al. (2016) have used SINS at the ALS to measure the very broadband plasmonic response of single doped metal oxide nanocrystals. They were able to carefully show that much narrower linewidths are observed in individual nanoparticles than the ensemble average as seen in far-field measurements of many nanoparticles together. These results indicate that sample heterogeneity is causing the anomalously large bandwidth and that the intrinsic damping of metal oxide localized surface plasmon resonances may be less than that of metal nanoparticles, allowing for the development of intriguing real-world applications.

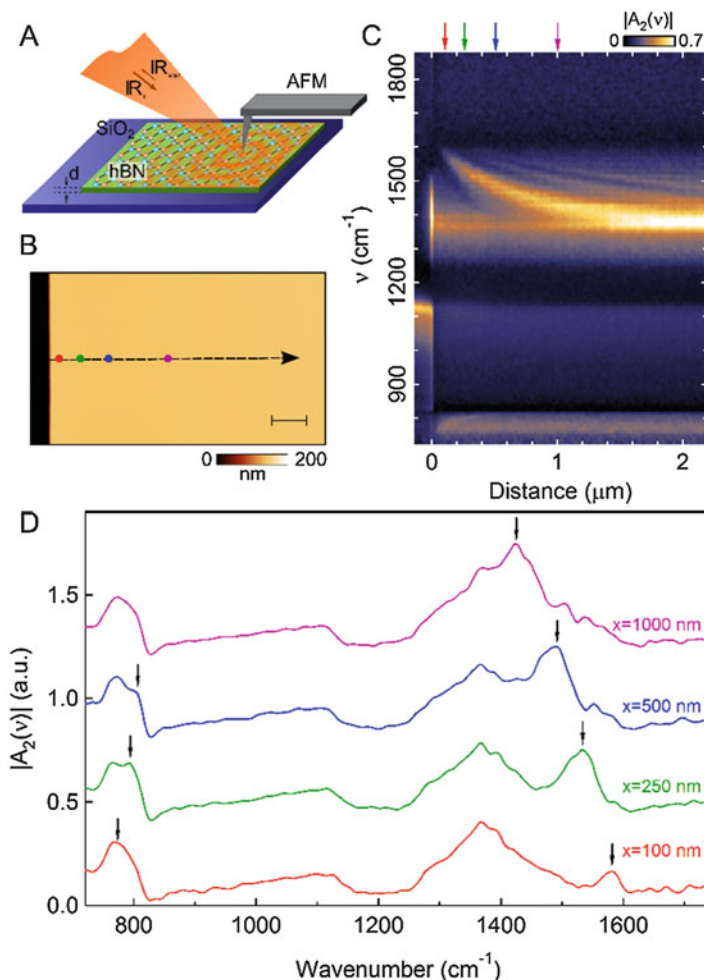


Fig. 37 Phonon polaritons observed in flakes of hexagonal boron nitride (hBN). As the AFM tip approaches the edge of the hBN flake, spatio-spectral SINS show that the out-of-plane 780 cm^{-1} and in-plane 1370 cm^{-1} phonon modes have a dispersing spectral feature which have opposite signs. (From Shi et al. 2015)

Measurements on single-nanoparticle catalysts (Wu et al. 2017) revealed chemical reactions on individual gold or platinum catalysts, showing enhancement of reactivity that is site-specific. Reactants and product distribution across the particles after exposure to oxidative or reductive conditions were studied with SINS at the ALS. They showed that the edges of the nanoparticles are indeed more chemically active than the middle flat regions, for the first time directly confirming the role of surfaces and reactive edges in nanoparticle catalysis (Fig. 38).

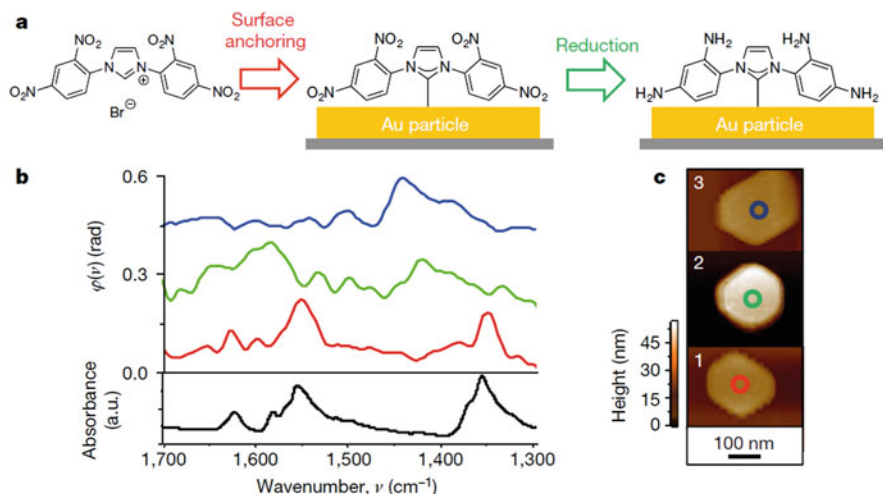


Fig. 38 Catalysis measured on individual catalytic particles. (From Wu et al. 2017)

References

- M. Abo-Bakr et al., Steady-state far-infrared coherent synchrotron radiation detected at BESSY II. *Phys. Rev. Lett.* **88**(25 Pt 1), 254801 (2002)
- M. Abo-Bakr et al., Brilliant, coherent far-infrared (THz) synchrotron radiation. *Phys. Rev. Lett.* **90**(9), 094801 (2003)
- M. Autore et al., Phase diagram and optical conductivity of $\text{La}_{1-x}\text{Eu}_{0.2}\text{Sr}_x\text{CuO}_4$. *Phys. Rev. B Condens. Matter* **90**(3), 035102 (2014)
- C.J. Baily, M. Surman, A.E. Russell, Investigation of the CO induced lifting of the (1×2) reconstruction on $\text{Pt}\{110\}$ using synchrotron far-infrared RAIRS. *Surf. Sci.* (2003). <https://www.sciencedirect.com/science/article/pii/S0039602802023464>
- J. Barros et al., Coherent synchrotron radiation for broadband terahertz spectroscopy. *Rev. Sci. Instrum.* **84**(3), 033102 (2013)
- D.N. Basov et al., Initial scientific uses of coherent synchrotron radiation in electron storage rings (2004). <https://escholarship.org/uc/item/7t33t36k>. Accessed 30 Mar 2018
- H.A. Bechtel, G.J. Flynn, C. Allen, Stardust interstellar preliminary examination III: infrared spectroscopic analysis of interstellar dust candidates. *Meteorit. Planet. Sci.* (2014a). <https://doi.org/10.1111/maps.12125/full>
- H.A. Bechtel, E.A. Muller, et al., Ultrabroadband infrared nanospectroscopic imaging. *Proc. Natl. Acad. Sci. U. S. A.* **111**, 7191–7196 (2014b). <https://doi.org/10.1073/pnas.1400502111>
- L. Bertrand et al., Cultural heritage and archaeology materials studied by synchrotron spectroscopy and imaging. *Appl. Phys. A Mater. Sci. Process.* **106**(2), 377–396 (2012)
- P. Born, K. Holldack, Analysis of granular packing structure by scattering of THz radiation. *Rev. Sci. Instrum.* **88**(5), 051802 (2017)
- R.A. Bosch, Shielding of infrared edge and synchrotron radiation. *Nucl. Instrum. Methods Phys. Res. Sect. A* **482**(3), 789–798 (2002)
- L. Bozec et al., Near-field photothermal Fourier transform infrared spectroscopy using synchrotron radiation. *Meas. Sci. Technol.* **13**, 1217–1222 (2002). <https://doi.org/10.1088/0957-0233/13/8/308>

- J.M. Byrd et al., Terahertz coherent synchrotron radiation from femtosecond laser modulation of the electron beam at the Advanced Light Source, Proceedings of the 2005 Particle Accelerator Conference, Knoxville, Tennessee (2005), pp. 3682–3684
- P. Calvani et al., Study of the optical gap in novel superconductors by coherent THz radiation. *Infrared Phys. Technol.* **51**(5), 429–432 (2008)
- G.L. Carr, Resolution limits for infrared microspectroscopy explored with synchrotron radiation. *Rev. Sci. Instrum.* **72**(3), 1613–1619 (2001)
- G. Carr, S. Kramer, J.B. Murphy, R.P.S.M. Lobo, D. Tanner, Observation of coherent synchrotron radiation from the NSLS VUV ring. *Nucl. Instrum. Methods Phys. Res. Sect. A* **463**, 387–392 (2001)
- G.L. Carr et al., High-power terahertz radiation from relativistic electrons. *Nature* **420**(6912), 153–156 (2002)
- G.L. Carr, O. Chubar, P. Dumas, Chapter 3, Multichannel detection with a synchrotron light source: design and potential, in *Spectrochemical Analysis Using Infrared Multichannel Detectors* 1st edn. (eds., Bhargava, R. and Levin, I.W.) 56–84 (Wiley-Blackwell, Oxford, 2007)
- J. Chen et al., Optical nano-imaging of gate-tunable graphene plasmons. *Nature* **487**, 77–81 (2012). <https://doi.org/10.1038/nature11254>
- O. Chubar et al., Physical optics computer code optimized for synchrotron radiation, in *Optical Design and Analysis Software II* Published in SPIE Proceedings Vol. 4769: Optical Design and Analysis Software II Richard C. Juergens, Editor(s) (2002), pp. 145–152. <https://doi.org/10.1117/12.481182>
- O. Chubar et al., Simulation and optimization of synchrotron infrared micro-spectroscopic beamlines using wave optics computation: ESRF and SOLEIL's cases. *AIP Conf. Proc.* (2007). <https://doi.org/10.1063/1.2436134>
- M. Cirtog et al., ... and Fourier transform infrared spectroscopy from neon matrix and a new supersonic jet experiment coupled to the infrared AILES beamline of synchrotron SOLEIL. *J. Phys. Chem. A* (2011). <https://doi.org/10.1021/jp111507z>
- M. Cotte et al., Recent applications and current trends in cultural heritage science using synchrotron-based Fourier transform infrared micro-spectroscopy. *C. R. Phys.* **10**(7) (2009). <https://doi.org/10.1016/j.crhy.2009.03.016>
- D. Creagh, J. McKinlay, P. Dumas, The design of the infrared beamline at the Australian synchrotron. *Vib. Spectrosc.* **41**(2) (2006). <https://doi.org/10.1016/j.vibspec.2006.02.009>
- A. Cvitkovic et al., Analytical model for quantitative prediction of material contrasts in scattering-type near-field optical microscopy. *Opt. Express* **15**, 8550–8565 (2007)
- J. D'Archangel et al., Near- and far-field spectroscopic imaging investigation of resonant square-loop infrared metasurfaces. *Opt. Express* **21**, 17150–17160 (2013). <https://doi.org/10.1364/oe.21.017150>
- S. Dai et al., Tunable phonon polaritons in atomically thin van der Waals crystals of boron nitride. *Science* **343**, 1125–1129 (2014). <https://doi.org/10.1126/science.1246833>
- A. Dazzi et al., Local infrared microspectroscopy with subwavelength spatial resolution with an atomic force microscope tip used as a photothermal sensor. *Opt. Lett.* **30**, 2388–2390 (2005). <https://doi.org/10.1364/ol.30.002388>
- P. Dumas et al., Adsorption and reactivity of NO on Cu(111): a synchrotron infrared reflection absorption spectroscopic study. *Surf. Sci.* **371**(2–3), 200 (1997)
- P. Dumas et al., Molecules at surfaces and interfaces studied using vibrational spectroscopies and related techniques. *Surf. Rev. Lett.* **6**(2), 225 (1999)
- W.D. Duncan, G.P. Williams, Infrared synchrotron radiation from electron storage rings. *Appl. Opt.* **22**(18), 2914–2923 (1983)
- U. Engström, R. Ryberg, Freezing out a Fermi resonance: a temperature dependence study of the low-energy modes of CO on Pt(111). *J. Chem. Phys.* **115**(1), 519–523 (2001)
- M. Faye et al., First high resolution analysis of the ν_3 band of the $^{36}\text{SF}_6$ isotopologue. *J. Mol. Spectrosc.* **346**, 23–26 (2018)
- Z. Fei et al., Gate-tuning of graphene plasmons revealed by infrared nano-imaging. *Nature* **487**, 82–85 (2012). <https://doi.org/10.1038/nature11253>

- L. Feng et al., Tip-enhanced infrared nanospectroscopy via molecular expansion force detection. *Nat. Photonics* **8**, 307–312 (2014). <https://doi.org/10.1038/nphoton.2013.373>
- R.O. Freitas et al., Infrared nanospectroscopy at the LNLs: current status and ongoing developments. *Synchrotron Radiat. News* **30**(4), 24–30 (2017). <https://doi.org/10.1080/08940886.2017.1338420>
- R.O. Freitas et al., Low-aberration beamline optics for synchrotron infrared nanospectroscopy. *Opt. Express* **26**, 11238–11249 (2018). <https://doi.org/10.1364/oe.26.011238>
- R. Georges et al., Nuclear spin symmetry conservation in H_2^{16}O investigated by direct absorption FTIR spectroscopy of water vapor cooled down in supersonic expansion. *J. Phys. Chem. A* **121**(40), 7455–7468 (2017)
- J.A. Gerber et al., Phase-resolved surface plasmon interferometry of graphene. *Phys. Rev. Lett.* **113** (2014). <https://doi.org/10.1103/PhysRevLett.113.055502>
- A.A. Govyadinov et al., Quantitative measurement of local infrared absorption and dielectric function with tip-enhanced near-field microscopy. *J. Phys. Chem. Lett.* **4**, 1526–1531 (2013)
- P.R. Griffiths, J.A. De Haseth, *Fourier Transform Infrared Spectrometry* (Wiley, New York, 1986)
- H. Günzler, H.-U. Gremlich, *IR Spectroscopy. An Introduction* (Wiley-VCH, Weinheim, 2002)
- A. Hecht, E. Zajac, *Optics*, 2nd edn. (Addison-Wesley, Reading, 1987)
- M. Hein et al., Friction of conduction electrons with adsorbates: simultaneous changes of DC resistance and broadband IR reflectance of thin Cu(111) films exposed to CO. *Surf. Sci.* **419**(2), 308–320 (1999)
- M. Hein et al., CO interaction with co-adsorbed C_2H_4 on Cu(111) as revealed by friction with the conduction electrons. *Surf. Sci.* **465**(3), 249–258 (2000)
- R.M. Herman et al., Rayleigh range and the M^2 factor for Bessel–Gauss beams. *Appl. Opt.* **37**(16), 3398–3400 (1998)
- P. Hermann et al., Near-field imaging and nano-Fourier-transform infrared spectroscopy using broadband synchrotron radiation. *Opt. Express* **21**, 2913–2919 (2013)
- C.J. Hirschmugl et al., Adsorbate-substrate resonant interactions observed for CO on Cu(100) in the far infrared. *Phys. Rev. Lett.* **65**(4), 480–483 (1990)
- A. Hofmann, Quasi-monochromatic synchrotron radiation from undulators. *Nucl. Inst. Methods* **152**(1), 17–21 (1978)
- V. Humblot et al., Synchrotron far-infrared RAIRS studies of complex molecules on Cu(110). *Surf. Sci.* **537**(1), 253–264 (2003)
- F. Huth et al., Infrared-spectroscopic nanoimaging with a thermal source. *Nat. Mater.* **10**, 352–356 (2011)
- F. Huth et al., Nano-FTIR absorption spectroscopy of molecular fingerprints at 20 nm spatial resolution. *Nano Lett.* **12**, 3973–3978 (2012)
- Y. Ikemoto et al., Development of scattering near-field optical microspectroscopy apparatus using an infrared synchrotron radiation source. *Opt. Commun.* **285**, 2212–2217 (2012)
- J.D. Jackson, *Classical Electrodynamics*, Third Edition (John Wiley and Sons, USA, 2007)
- R.W. Johns et al., Direct observation of narrow mid-infrared plasmon linewidths of single metal oxide nanocrystals. *Nat. Commun.* **7** (2016). <https://doi.org/10.1038/ncomms11583>
- F. Keilmann, R. Hillenbrand, Near-field microscopy by elastic light scattering from a tip. *Philos. Trans. R. Soc. Lond. Ser. A Math. Phys. Eng. Sci.* **362**, 787–805 (2004). <https://doi.org/10.1098/rsta.2003.1347>
- O. Khatib et al., Far infrared synchrotron near-field nanoimaging and nanospectroscopy. *ACS Photonics* **5**, 2773–2779 (2018). <https://doi.org/10.1021/acsphotonics.8b00565>
- A.M. Khounsary, B. Lai, *Power Distributions of the APS Bending Magnets and Insertion Devices*. Argonne Light Source Note LS-198 (1992). https://www.aps.anl.gov/icms_files/lnotes/files/APS_1417922.pdf
- S. Kimura et al., Front end and optics of infrared beamline at SPring-8. *Nucl. Instrum. Methods Phys. Res. Sect. A* **467–468**(Part 1), 437–440 (2001)
- B. Knoll, F. Keilmann, Near-field probing of vibrational absorption for chemical microscopy. *Nature* **399**, 134–137 (1999). <https://doi.org/10.1038/20154>

- F. Kwabia Tchana et al., A new, low temperature long-pass cell for mid-infrared to terahertz spectroscopy and synchrotron radiation use. *Rev. Sci. Instrum.* **84**(9), 093101 (2013)
- P. Lagarde, Infrared spectroscopy with synchrotron radiation. *Infrared Phys.* (1978). [https://doi.org/10.1016/0020-0891\(78\)90046-5](https://doi.org/10.1016/0020-0891(78)90046-5)
- P. Lerch et al., Assessing noise sources at synchrotron infrared ports. *J. Synchrotron Radiat.* **19**(Pt 1), 1–9 (2012)
- Z.Q. Li et al., Band structure asymmetry of bilayer graphene revealed by infrared spectroscopy. *Phys. Rev. Lett.* **102**(3), 037403 (2009)
- M. Liu et al., Phase transition in bulk single crystals and thin films of VO₂ by nanoscale infrared spectroscopy and imaging. *Phys. Rev. B* **91**, 245155 (2015)
- I. Lo Vecchio et al., Optical conductivity of V₄O₇ across its metal-insulator transition. *Phys. Rev. B Condens. Matter* **90**(11), 115149 (2014)
- R. López-Delgado, H. Szwarc, Focusing all the synchrotron radiation (2 π radians) from an electron storage ring on a single point without time distortion. *Opt. Commun.* **19**(2), 286–291 (1976)
- K. Loutherbach et al., Microfluidic approaches to synchrotron radiation-based Fourier transform infrared (SR-FTIR) spectral microscopy of living biosystems. *Protein Pept. Lett.* **23**(3), 273–282 (2016)
- M.C. Martin, P. Dumas, Materials sciences using synchrotron infrared light sources, in *Spectroscopic Properties of Inorganic and Organometallic Compounds: Techniques, Materials and Applications*, ed. by J. Yarwood, R. Douthwaite, S. Duckett, vol. 43 (Royal Society of Chemistry, Cambridge, 2012), pp. 141–165
- D.H. Martin, E. Puplett, Polarised interferometric spectrometry for the millimetre and submillimetre spectrum. *Infrared Phys.* **10**(2), 105–109 (1970)
- M.C. Martin et al., Negligible sample heating from synchrotron infrared beam. *Appl. Spectrosc.* (2001). <https://doi.org/10.1366/0003702011951551>
- M.C. Martin et al., Recent applications and current trends in analytical chemistry using synchrotron-based Fourier-transform infrared microspectroscopy. *TrAC Trends Anal. Chem.* **29**(6) (2010). <https://doi.org/10.1016/j.trac.2010.03.002>
- E.C. Mattson et al., Restoration and spectral recovery of mid-infrared chemical images. *Anal. Chem.* **84**, 6173–6180 (2012). <https://doi.org/10.1021/ac301080h>
- T.E. May, Infrared facility at the Canadian light source. *Infrared Phys. Technol.* **45**(5), 383–387 (2004)
- A.R.W. McKellar, High-resolution infrared spectroscopy with synchrotron sources. *J. Mol. Spectrosc.* **262**(1), 1–10 (2010)
- A.S. McLeod et al., Model for quantitative tip-enhanced spectroscopy and the extraction of nanoscale-resolved optical constants. *Phys. Rev. B* **90** (2014). <https://doi.org/10.1103/PhysRevB.90.085136>
- P. Meyer, P. Lagarde, Synchrotron radiation in the infrared. *J. Phys.* **37**(12), 1387–1390 (1976)
- L.M. Miller, P. Dumas, From structure to cellular mechanism with infrared microspectroscopy. *Curr. Opin. Struct. Biol.* **20**(5) (2010). <https://doi.org/10.1016/j.sbi.2010.07.007>
- C. Mirri et al., Anisotropic optical conductivity of Sr₄Ru₃O₁₀. *Phys. Rev. B Condens. Matter* **85**(23), 235124 (2012)
- E. Mitri et al., SU-8 bonding protocol for the fabrication of microfluidic devices dedicated to FTIR microspectroscopy of live cells. *Lab Chip* **14**(1) (2014). <https://doi.org/10.1039/c3lc50878a>
- T. Moreno, Optimized IR synchrotron beamline design. *J. Synchrotron Radiat.* **22**(5), 1163–1169 (2015)
- T. Moreno, M. Idir, SPOTX a ray tracing software for X-ray optics. *J. Phys. IV* **11**(PR2), Pr2–527–Pr2–531 (2001)
- T. Moreno et al., Optical layouts for large infrared beamline opening angles. *J. Phys. Conf. Ser.* **424**(Part 4), 55–56 (2013)
- E.A. Muller et al., Infrared chemical nano-imaging: accessing structure, coupling, and dynamics on molecular length scales. *J. Phys. Chem. Lett.* **6**, 1275–1284 (2015)
- T. Nanba et al., Far-infrared spectroscopy by synchrotron radiation at the UVSOR facility. *Int. J. Infrared Millimeter Waves* **7**(11), 1769–1776 (1986)

- M.J. Nasse et al., High-resolution Fourier-transform infrared chemical imaging with multiple synchrotron beams. *Nat. Methods* **8**(5), 413–416 (2011). <https://doi.org/10.1038/nmeth.1585>
- J. Nehr Korn et al., Recent progress in synchrotron-based frequency-domain Fourier-transform THz-EPR. *J. Magn. Reson.* **280**, 10–19 (2017)
- B. Nelander, The beam line for infrared spectroscopy at the Lund University synchrotron radiation source. *J. Mol. Struct.* **294**, 205 (1993)
- B. Nelander, V. Sablinskas, Status report from the beam line for IR spectroscopy at Max-lab. *J. Mol. Struct.* **348**, 167–169 (1995)
- J.S. Nodvick, D.S. Saxon, Suppression of coherent radiation by electrons in a synchrotron. *Phys. Rev. J. Arch.* **96**, 180 (1954)
- P.R. Norton, Infrared image sensors. *Organ. Ethics Healthc. Bus. Policy OE* **30**(11), 1649–1664 (1991)
- A. Nucara et al., Hardening of the soft phonon in bulk SrTiO₃ interfaced with LaAlO₃ and SrRuO₃. *Phys. Rev. B Condens. Matter* **93**(22), 224103 (2016)
- J. Pellicer-Porres et al., High-pressure study of the infrared active modes in wurtzite and rocksalt ZnO. *Phys. Rev. B* **84**(12) (2011). <https://doi.org/10.1103/PhysRevB.84.125202>
- J. Pellicer-Porres et al., Investigation of lattice dynamical and dielectric properties of MgO under high pressure by means of mid- and far-infrared spectroscopy. *J. Phys. Condens. Matter* **25**(50) (2013). <https://doi.org/10.1088/0953-8984/25/50/505902>
- F. Peragut et al., Infrared near-field imaging and spectroscopy based on thermal or synchrotron radiation. *Appl. Phys. Lett.* **104** (2014). <https://doi.org/10.1063/1.4885416>
- B.N.J. Persson, A.I. Volokitin, Infrared reflection-absorption spectroscopy of dipole-forbidden adsorbate vibrations. *Surf. Sci.* **310**(1), 314–336 (1994)
- A. Perucchi et al., Multiband conductivity and a multigap superconducting phase in V₃Si films from optical measurements at terahertz frequencies. *Phys. Rev. B Condens. Matter* **81**(9), 092509 (2010)
- B. Pollard et al., Infrared vibrational nanospectroscopy by self-referenced interferometry. *Nano Lett.* **16**, 55–61 (2016). <https://doi.org/10.1021/acs.nanolett.5b02730>
- M. Quack, F. Merkt, *Handbook of High-Resolution Spectroscopy*, vol. 2 (Wiley, Chichester, 2011), pp. 965–1019. Chapter 26
- A. Rogalski, Infrared detectors: an overview. *Infrared Phys. Technol.* **43**(3), 187–210 (2002)
- A. Rogalski, Infrared detectors: status and trends. *Prog. Quantum Electron.* **27**(2), 59–210 (2003)
- P. Roy et al., Infrared synchrotron radiation from an undulator. *Nucl. Instrum. Methods Phys. Res. Sect. A* **325**(3), 568–573 (1993)
- P. Roy et al., The AILES infrared beamline on the third generation synchrotron radiation facility SOLEIL. *Infrared Phys. Technol.* **49**(1), 139–146 (2006)
- E.L. Runnerstrom et al., Defect engineering in plasmonic metal oxide nanocrystals. *Nano Lett.* **16**, 3390–3398 (2016). <https://doi.org/10.1021/acs.nanolett.6b01171>
- N. Salvadó et al., Advantages of the use of SR-FTIR microspectroscopy: applications to cultural heritage. *Anal. Chem.* **77**(11), 3444–3451 (2005)
- U. Schade et al., THz near-field imaging employing synchrotron radiation. *Appl. Phys. Lett.* **84**, 1422–1424 (2004). <https://doi.org/10.1063/1.1650034>
- U. Schade et al., THz near-field imaging of biological tissues employing synchrotron radiation. *Proc. SPIE Int. Soc. Opt. Eng.* **5725**, 46–52 (2005). <https://doi.org/10.1117/12.590731>
- E. Schweizer et al., The electron storage ring as a source of infrared radiation. *Nucl. Instrum. Methods Phys. Res. Sect. A* **239**(3), 630–634 (1985)
- J. Schwinger, On the classical radiation of accelerated electrons. *Phys. Rev.* **75**(12), 1912–1925 (1949)
- Z. Shi et al., Amplitude- and phase-resolved nanospectral imaging of phonon polaritons in hexagonal boron nitride. *ACS Photonics* **2**, 790–796 (2015). <https://doi.org/10.1021/acsphotonics.5b00007>
- M. Shimada et al., Intense terahertz synchrotron radiation by laser bunch slicing at UVSOR-II electron storage ring. *Jpn. J. Appl. Phys.* **46**, 7939 (2007)

- A. Shurakov, Y. Lobanov, Superconducting hot-electron bolometer: from the discovery of hot-electrons phenomena to practical applications. *Supercond. Sci. Technol.* **29**(2), 023001 (2015)
- E.J. Singley et al., Measuring the Josephson plasma resonance in $\text{Bi}_2\text{Sr}_2\text{CaCu}_2\text{O}_8$ using intense coherent THz synchrotron radiation. *Phys. Rev. B Condens. Matter* **69**(9), 092512 (2004)
- E. Stavitski et al., Dynamic full-field infrared imaging with multiple synchrotron beams. *Anal. Chem.* **85**, 3599–3605 (2013). <https://doi.org/10.1021/ac3033849>
- D. Steele, Infrared spectroscopy: theory, in *Handbook of Vibrational Spectroscopy*, ed. by J. M. Chalmers, vol. 1 (Wiley, Chichester, 2002), pp. 44–70
- J.R. Stevenson, J.M. Cathcart, Design considerations for parasitic use of synchrotron radiation in the infrared. *Nucl. Inst. Methods* **172**(1), 367–369 (1980)
- J.R. Stevenson, H. Ellis, R. Bartlett, Synchrotron radiation as an infrared source. *Appl. Opt.* **12**(12), 2884–2889 (1973)
- B.H. Stuart, *Infrared Spectroscopy: Fundamentals and Applications* (Wiley, 2004). <http://www.kinetics.nsc.ru/chichinin/books/spectroscopy/Stuart04.pdf>
- M. Surman et al., Adsorption of CO on $\text{Pt}\{1\ 1\ 1\}$: a synchrotron far-infrared RAIRS study. *Surf. Sci.* **511**(1–3), L303–L306 (2002)
- S. Tammaro et al., High density terahertz frequency comb produced by coherent synchrotron radiation. *Nat. Commun.* **6**, 7733 (2015)
- L. Vaccari et al., Infrared microspectroscopy of live cells in microfluidic devices (MD-IRMS): toward a powerful label-free cell-based assay. *Anal. Chem.* **84**(11), 4768–4775 (2012)
- H. Wiedemann, Charged particle acceleration, in *Particle Accelerator Physics: Basic Principles and Linear Beam Dynamics*, ed. by H. Wiedemann (Springer Berlin Heidelberg, Berlin/Heidelberg, 1993), pp. 265–299
- G.P. Williams, The national synchrotron light source in the infrared region. *Nucl. Instrum. Methods Phys. Res.* **195**(1), 383–387 (1982)
- C.-Y. Wu et al., High-spatial-resolution mapping of catalytic reactions on single particles. *Nature* **541**, 511–515 (2017). <https://doi.org/10.1038/nature20795>